THE JOURNAL OF PHYSICAL CHEMISTRY A
A JOURNAL OF THE AMERICAN CHEMICAL SOCIETY

pubs.acs.org/JPCA Article

# Triple Emission of 5′-(*para*-R-Phenylene)vinylene-2-(2′-hydroxyphenyl)benzoxazole (PVHBO). Part I: Dual Emission from the Neutral Species

Quinton J. Meisner,[‖] Joseph J. M. Hurley,[‖] Peijun Guo, Anna R. Blood, Richard D. Schaller, David J. Gosztola, Gary P. Wiederrecht, and Lei Zhu*

Cite This: *J. Phys. Chem. A* 2022, 126, 1033−1061 Read Online



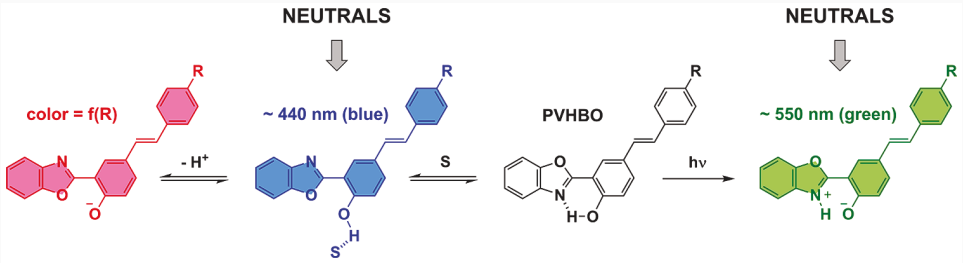


**ABSTRACT:** The effects of 5′-(*para*-R-phenylene)vinylene (PV) substituents on the emission properties of 2-(2′-hydroxyphenyl)-benzoxazole (HBO) are analyzed using steady-state and time-resolved absorption and emission spectroscopies in addition to quantum chemical calculations. All members in the series of **PVHBO**s are capable of excited-state intramolecular proton transfer (ESIPT) with a solvent sensitivity that is typical of a HBO derivative to produce a normal (aka enol) emission and an excited-state tautomer (aka keto) emission. These two emission bands of the neutral dyes are discussed in the current paper. The intermolecular proton transfer, i.e., the deprotonation, of a **PVHBO** results in the third band of the triple emission, which is described in the succeeding paper. The placement of an electron-withdrawing substituent R on the **PVHBO** scaffold increases the intensity of the keto emission relative to the enol emission in hydrogen-bonding solvents. The R substituents do not significantly alter the wavelengths of the enol and keto emission bands, which are located in the blue and green regions, respectively, of the visible spectrum. The ultrafast time-resolved spectroscopies and quantum chemical calculations offer explanations on how the R group and the solvent affect the enol and keto emission properties (i.e., wavelength, lifetime, fluorescence quantum yield, and relative ratio of their emissions). The key findings include the following: (1) the emission energies of both enol and keto forms are not sensitively dependent on the R substituent and (2) the solvent-engaged enol excited state is quenched more efficiently as the R substituent becomes more electron-withdrawing. A **PVHBO** acts as a fusion of HBO and stilbenoid that intersect at the hydroxyphenyl moiety. Depending on the solvent and other environmental conditions, **PVHBO**s may exhibit the ESIPT property of HBO or the substituent-dependent emission of stilbenoid. This paper and the succeeding article provide a photophysical model of **PVHBO**s to explain the wavelengths and relative abundances of the three emission bands (enol, keto, and anion) that these compounds are able to produce. Judicial selection of the environmental factors may drive the emission of a **PVHBO** into the spectral regions of blue, green, and, in a couple of cases, orange or red.



## INTRODUCTION

2-(2′-Hydroxyphenyl)benzoxazole (HBO; Figure 1) is capable of undergoing excited-state intramolecular proton transfer (ESIPT) and producing dual emission from normal (enol) and proton-transferred (keto) species.[1,2] HBO can also be deprotonated to produce the third emissive species, the conjugate base, which has an emission band between those of the enol and keto forms (Figure 1).[2,3] HBO occupies a special place in organic photochemistry because it is a simple structure of which the excited-state proton transfer reactions and the resulting multiple emissions have been thoroughly characterized, both experimentally and theoretically.[1,2,4−11] HBO has also been decorated in a myriad of manners while maintaining its core capacity of ESIPT to produce fundamentally interesting but also prospectively functional molecules as fluorescent probes or emitters in optoelectronic devices.[12−15] The three emission bands of the unsubstituted HBO are

Received: November 29, 2021
Revised: January 24, 2022
Published: February 10, 2022

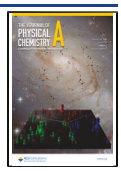





https://doi.org/10.1021/acs.jpca.1c10165
*J. Phys. Chem. A* 2022, 126, 1033−1061

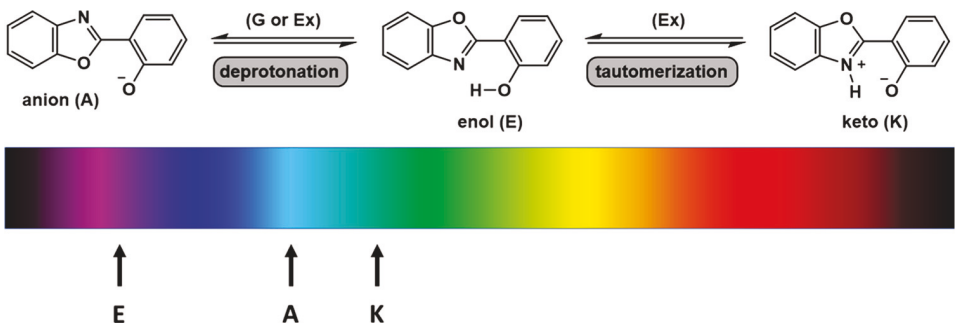


**Figure 1.** Three emission bands of HBO: enol (i.e., normal, E), keto (i.e., tautomer, K), and anion (A). G and Ex are ground and excited states, respectively.

clustered in the UV/blue region of the electromagnetic spectrum (Figure 1). The question that we wish to answer in this work is how a systematic alteration of the HBO structure in conjunction with the effect of solvation could produce emissions at the three primary colors (R, G, B) in the visible spectrum while maintaining or exceeding the emission yields and brightness of HBO. Although the resulting molecules might be useful as the emitters in organic light-emitting devices (OLEDs),[16−18] the present focus is entirely on the interpretations of the spectroscopic observations from the topical compounds, from which their emission behaviors can be understood and predictions may be made on the effects of other functionalizations on HBO or on similar ESIPT-capable compounds.

The normal emission from the enol form ("E" in Figure 1) of HBO centers at ∼370 nm in a hydrogen-bonding solvent, while the tautomer emission from the keto form (K) peaking at 475 nm is dominant, if not exclusive, in solvents such as dichloromethane (DCM) that preserve the intramolecular hydrogen bond (HB).[2] The excitation spectrum of the keto form is slightly red-shifted from that of the enol (in a solvent that would produce both emissions), which suggests that certain ground-state species are more prone to ESIPT than others.[19] Upon deprotonation with a base in DMSO, the center of the lowest-energy absorption band of HBO shifts from 320−330 nm to near 400 nm,[2] while the maximum of the emission is 450 nm (A).[2] It is noteworthy that the emission of the anion falls between those of enol and keto forms (Figure 1), which will be discussed in the succeeding paper.[20] These three emission bands are found in the near-UV and blue regions. In the current work, the structural modification was made to move these three bands, enol, keto, and anion, to achieve a larger collective coverage of the visible spectrum. This paper describes the properties of the HBO derivatives in their neutral forms, while the succeeding paper[20] covers the conjugate bases (anions) of these compounds.

## METHODS

The synthetic procedures along with the characterization data of **PVHBO**s are included in the Supporting Information. The major spectroscopic methods are picosecond time-resolved emission spectroscopy and femtosecond time-resolved transient absorption spectroscopy. The quantum chemical calculations were carried out using the software package Turbomole.

**Picosecond Time-Resolved Emission Spectroscopy.** The data were acquired at Argonne National Laboratory at the Center of Nanoscale Materials user facility. This system utilizes a Hamamatsu C5680 streak camera system, synchronized with the output of an amplified femtosecond laser system (Newport Spectra Physics) coupled to an optical parametric amplifier (OPA). The OPA output, which serves as the ultrafast pump light, was set at 310 nm. The temporal resolution of the streak camera is 2 ps. The photons collected within a time slice (e.g., 6−16 ps) over the whole spectral range, or a wavelength slice (e.g., 570−560 nm) over time, were extracted using the software High Performance Digital Temporal Analyzer (HPD-TA 8). The multiexponential fittings of the time decay data were done in Origin 2020 using the provided ExpDecay functions.

**Femtosecond Time-Resolved Transient Absorption Spectroscopy.** The transient absorption data were acquired at Argonne National Laboratory in the Center for Nanoscale Materials user facility. The system is an amplified femtosecond Ti:sapphire laser system operating at 5 kHz and with a center wavelength of 800 nm. The output of the amplifier is split, with 95% of the output directed to pump an optical parametric amplifier (OPA), providing tunable output in the UV, visible, and near-infrared spectral ranges. The output of the OPA serves as the pump light. The remaining 5% is focused onto a 2 mm thick sapphire crystal to create a broad, white light continuum pulse that serves as the probe. The probe is sent down a variable delay line, while the pump light is chopped at 2.5 kHz (half the laser repetition rate). A depolarizer is also present in the pump beam to avoid contributions to the transient signal other than that due to population (e.g., avoiding molecular birefringence). The beams are overlapped in the sample, with the probe light after the sample coupled to a spectrograph via an optical fiber. With each position of the optical delay line, a transient spectrum from 450 to 750 nm is acquired, with typical averaging per delay point of more than 10 000 pulses. In these experiments, the pump wavelength was 310 nm. The samples were (relatively) photostable at a pump power of 200 $\mu$W, which we can discern because for repeat scans (3), the scans have the same amplitude and kinetic features. The kinetic traces were synced at time zero (time zero correction) before fitted using the multiexponential function in Surface Xplorer. The time constants fitted with the IRF fixed at 130 fs were included in the tables (while a floating IRF generally gave better fits than using a fixed IRF, a floating IRF could masquerade the fast rise component(s). Therefore, the data referred to in the paper were determined using the 130 fs IRF). For traces of complicated multiple-component decays, at most five time constants were used and fitted in the following manner: the IRF was set at 0.13 ps. The five time constants were generally restricted in the following regions: $t_1$ (0−0.5


https://doi.org/10.1021/acs.jpca.1c10165
J. Phys. Chem. A 2022, 126, 1033−1061

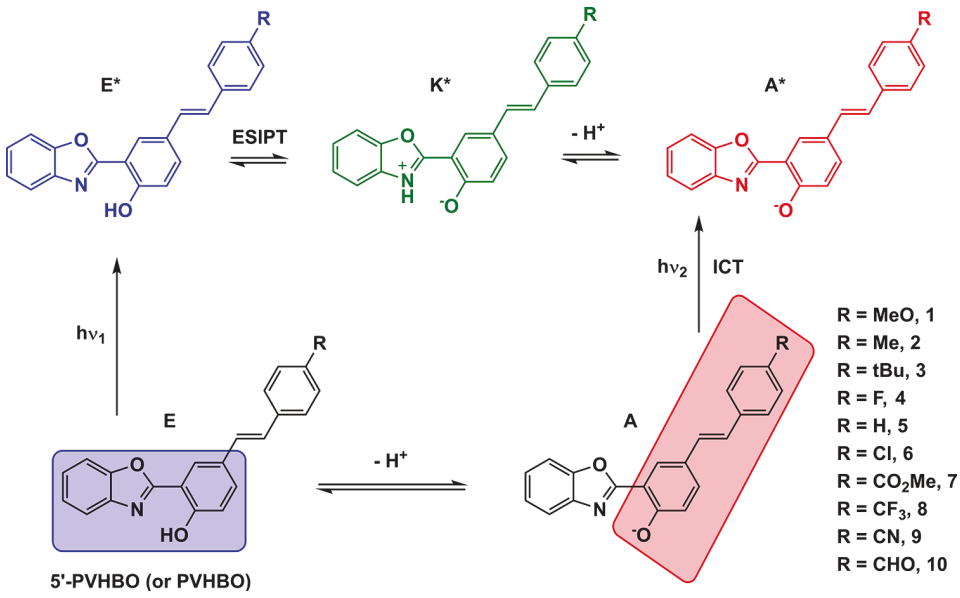


**Figure 2.** Postulated effect of substitution at the 5′-position of HBO with a phenylenevinylene (PV) group. The HBO and deprotonated stilbenoid fluorophores are boxed in blue and red, respectively. The colors included in the structures on the excited-state level represent the emission colors of the respective species when the R group is e-withdrawing.

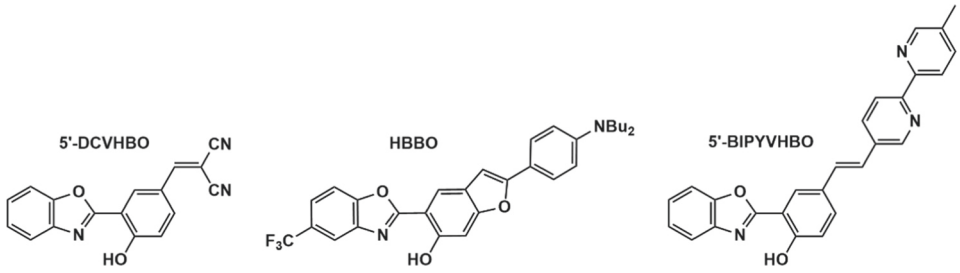


**Figure 3.** Three examples of 5′-substituted HBO.

ps), $t_2$ (0.13−1 ps), $t_3$ (1−10 ps), $t_4$ (10−100 ps), and $t_5$ (>100 ps). Initial values and signs of amplitudes (if needed) were selected based on the visual inspection of the decay curve. If any of the component was fitted to a boundary value, the range was expanded and fitted again. If one component was fitted with a negligible amplitude value, that component was removed, and the decay data were fitted again.

**Quantum Chemical Calculations.** All calculations were carried out using the quantum chemistry package TURBOMOLE V7.4.[21] The ground-state geometries were optimized at the density functional level of theory (DFT) using the B3LYP functional[22] and the def2-TZVP basis sets.[23] The second derivatives were calculated using the "aoforce" module to confirm the nature of the stationary points to be either minima or transition states. The excited-state geometric and electronic structural parameters were determined using the time-dependent DFT (TDDFT)[24] with the same functional and basis sets as listed above. The second derivatives of the minimized geometries in the excited states were calculated using the "NumForce" module to distinguish between minima and transition states. When calculating the minimal energy reaction paths, the smaller basis sets def2-SV(P) were used to reduce the computational cost. The frontier molecular orbitals were plotted using gOpenMol.[25,26] The excitation energies were calculated using both TDDFT/B3LYP and the CC2 methods[27,28] with the resolution-of-the-identity (RI) approximation. When needed, the COSMO (COnductor-like Screening MOdel) solvation model[29] was applied in the optimization of structures in DMSO.

## RESULTS

**Molecular Design.** Placing a phenylenevinylene (PV) substituent on the 5′-position of HBO creates what we refer to as a **PVHBO** (Figure 2), in which two fluorophores, HBO and the hydroxy-substituted stilbene (stilbenoid), meet at a phenyl ring. A neutral **PVHBO** molecule is expected to exhibit the ESIPT behavior inherited from the HBO component, while the photophysical characteristics of the stilbenoid moiety are amplified in the deprotonated form.

There are numerous reports on the chemistry of substituted HBOs,[30,31] a few of which contain substituents at the 5′-positions. Three examples are shown in Figure 3. **5′-DCVHBO** was described as the reporter of a Pd(II)-sensitive probe.[32] The photophysical properties of this molecule and its conjugated base have not been characterized thoroughly. **HBBO** was reported to have balanced enol and keto emissions, which lead to an overall white emission.[33] Our group studied the excitation- and solvent-dependent multiple emissions of **5′-BIPYVHBO**,[19] which bears the design of two orthogonal electronic transitions merging at the hydroxyphenyl component. Depending on the protonation status of the ground state, one excited-state consequence would manifest itself over the


https://doi.org/10.1021/acs.jpca.1c10165
J. Phys. Chem. A 2022, 126, 1033−1061

**Scheme 1. Synthesis of PVHBOs**[a,b]

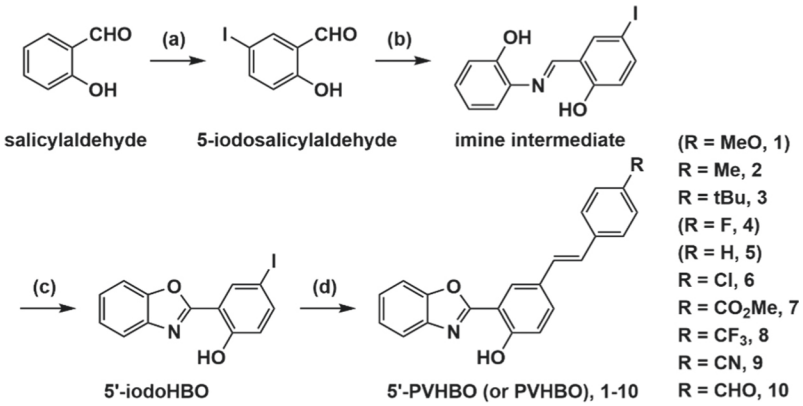


[a]Reagents and conditions: (a) NIS, TFA, rt, 3 h, 67%; (b) 2-aminophenol, ethanol (200 proof), 0 °C—rt, 3 h, 67%; (c) methanol, $PhI(OAc)_2$, rt, 3 h, 70%; and (d) 4-R-styrene, $Pd(OAc)_2$, $(p\text{-tolyl})_3P$, $Et_3N$, DMF, 100 °C, overnight, depending on R, 16–69%. [b]The compounds that were prepared with a different approach (see Scheme S1 in the SI) are indicated by parentheses.

**Table 1. Absorption Maxima (nm) of Compounds 1–10 in Five Solvents (DCM, ACN, EtOH, DMF, DMSO)**[a]

| Comp. # | R-Group | $\sigma_p^+$ | δ(OH)/ppm | DCM | ACN | EtOH | DMF | DMSO |
|---|---|---|---|---|---|---|---|---|
| **1** | OMe | -0.78 | 11.50 | 307 | 307 | 307 | 307 | 310 |
| **2** | Me | -0.31 | 11.55 | 308 | 305 | 305 | 313 | 315 |
| **3** | t-Bu | -0.26 | 11.55 | 308 | 309 | 307 | 316 | 316 |
| **4** | F | -0.07 | 11.56 | 307 | 304 | 305 | 308 | 309 |
| **5** | H | 0 | 11.56 | 309 | 308 | 307 | 312 | 312 |
| **6** | Cl | 0.11 | 11.52 | 307 | 306 | 305 | 308 | 308 |
| **7** | $CO_2CH_3$ | 0.49 | 11.63 | 334 | 329 | 331 | 336 | 338 |
| **8** | $CF_3$ | 0.61 | 11.55 | 307 | 306 | 306 | 309 | 311 |
| **9** | CN | 0.66 | 11.68 | 336 | 330 | 332 | 335 | 338 |
| **10** | CHO | 0.73 | 11.66 | 349 | 343 | 345 | 345 | 351 |

[a]The rows of Group II (see text) compounds are shaded. The Hammett constants ($\sigma_p^+$) and chemical shifts ($\delta$) of the hydroxy in $CDCl_3$ are also listed as ground-state properties.

other (i.e., ESIPT of neutral vs CT (charge transfer) of the anion). The effectiveness of leveraging orthogonal electronic transitions in materializing multiple emissions was tested in the single case of **5′-BIPYVHBO**.[19] In the current work, we present a systematic analysis on how the electronic nature of the substituent on the phenyl of a **PVHBO** affects the wavelengths and relative proportions of the three emission bands—enol (E), keto (K), and anion (A). The properties of **PVHBO**s in neutral forms are reported in this paper, while the chemistry of the anions is described in the succeeding article.[20]

**Synthesis.** The synthesis of most **PVHBO**s is illustrated in Scheme 1. 5-Iodosalicylaldehyde, while commercially available, is prepared conveniently via iodination of salicylaldehyde using *N*-iodosuccinimide (NIS) in trifluoroacetic acid (TFA).[34] The subsequent oxidative cyclization with 2-aminophenol affords 5′-iodoHBO. Heck reactions between 5′-iodoHBO and various substituted styrenes produce the target compounds. Compounds **1**, **4**, and **5** were prepared using a different approach, which is described in the SI (Scheme S1). The compounds are numbered in the ascending order of Hammett


https://doi.org/10.1021/acs.jpca.1c10165
J. Phys. Chem. A 2022, 126, 1033–1061

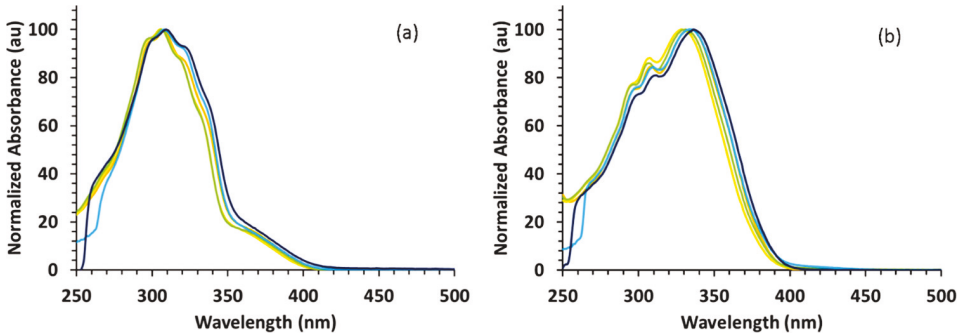


**Figure 4.** Normalized absorption spectra of **1** (R = MeO, a) and **9** (R = CN, b) in DCM (orange), ACN (yellow), EtOH (green), DMF (cyan), and DMSO (navy); [dye] = 15 $\mu$M. The UV cutoffs of DMF and DMSO are at 270 and 268 nm, respectively.

**Table 2. Fluorescence Emission Wavelength Maxima (in nm) of the Enol Band of PVHBOs in DCM, ACN, EtOH, DMF, and DMSO[c]**

| Comp. # | R-Group | DCM | ACN | EtOH | DMF | DMSO |
|---|---|---|---|---|---|---|
| **1** | OMe | N/A[a] | S[b] | 437 | 435 | 443 |
| **2** | Me | N/A | 423 | 430 | 428 | 427 |
| **3** | t-Bu | N/A | S | 425 | 422 | 426 |
| **4** | F | N/A | 419 | 423 | 418 | 422 |
| **5** | H | N/A | 421 | 422 | 419 | 421 |
| **6** | Cl | N/A | 418 | 420 | 419 | 422 |
| **7** | $CO_2CH_3$ | N/A | N/A | S | 440 | 454 |
| **8** | $CF_3$ | N/A | S | 412 | 412 | 416 |
| **9** | CN | N/A | S | S | 432 | 437 |
| **10** | CHO | N/A | N/A | S | S | S |

[a]N/A, not observed. [b]S, shoulder. [c]The rows of Group II compounds are shaded.

($\sigma_p^+$) values[35] of the R substituents. The **PVHBO**s are emissive in the solid state. Most of them emit green light (Figure S1). The X-ray single-crystal structure of one of the compounds (**5**; Figure S2) reveals the intact intramolecular HB in the HBO component, suggesting that the solid-state emission comes from the keto form after ESIPT.

The chemical shifts of the OH of **PVHBO**s are over 11.5 ppm in $CDCl_3$ (Table 1), consistent with the presence of intramolecular HBs. The chemical shift values are close to one another in this series of compounds, although those of **7**, **9**, and **10** are slightly and consistently larger than the rest. Based on the works by Chou and others that relate the ground-state intramolecular HB strengths, as inferred from the OH chemical shift values, to the efficiency of ESIPT of intramolecularly hydrogen-bonded dyes,[36−39] hypothesis could be advanced in the current case that compounds **7**, **9**, and **10** are more inclined to produce the emission from the proton-transferred tautomers in the excited state.

**Absorption.** The steady-state absorption spectra of **PVHBO**s were obtained in five solvents—dichloromethane (DCM), acetonitrile (ACN), ethanol (EtOH), DMF, and DMSO. For each compound, small differences between solvents were observed, where the spectra in DMF and DMSO were (only slightly) bathochromically shifted from the rest. The maxima of absorption are listed in Table 1, although the major spectral difference across the **PVHBO** series lies in the spectral line shapes of the spectra, based on which the **PVHBO** compounds are divided into two groups. Group I includes **1**−**6** and **8** (R = OMe, Me, *t*Bu, F, H, Cl, and $CF_3$, respectively). The absorption spectra in this group have


https://doi.org/10.1021/acs.jpca.1c10165
J. Phys. Chem. A 2022, 126, 1033−1061

Table 3. Fluorescence Emission Wavelength Maxima (in nm) of the Keto Band of PVHBOs in DCM, ACN, EtOH, DMF, and DMSO[b]

| Comp. # | R-Group | DCM | ACN | EtOH | DMF | DMSO |
|---|---|---|---|---|---|---|
| **1** | OMe | 549 | 548 | 548 | 552 | S[a] |
| **2** | Me | 548 | 545 | 544 | 547 | S |
| **3** | t-Bu | 547 | 545 | 544 | 547 | S |
| **4** | F | 545 | 540 | 539 | 541 | S |
| **5** | H | 542 | 543 | 542 | 543 | S |
| **6** | Cl | 542 | 542 | 540 | 541 | S |
| **7** | $CO_2CH_3$ | 540 | 540 | 540 | 547 | 548 |
| **8** | $CF_3$ | 535 | 536 | 535 | 540 | 543 |
| **9** | CN | 539 | 538 | 539 | 546 | 549 |
| **10** | CHO | 542 | 544 | 549 | 548 | 553 |

[a]S, shoulder. [b]The rows of Group II compounds are shaded.

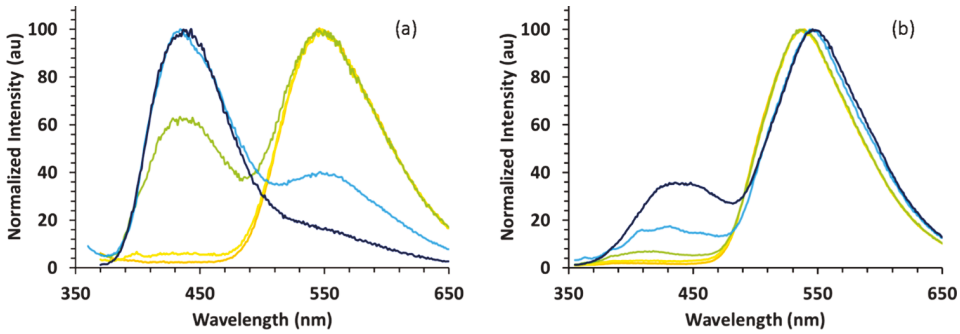


**Figure 5.** Normalized fluorescence spectra of **1** (a, R = MeO, $\lambda_{ex}$ = 330 nm) and **9** (b, $\lambda_{ex}$ = 345 nm) in DCM (orange), ACN (yellow), EtOH (green), DMF (cyan), and DMSO (navy); [dye] = 15 $\mu$M.

maxima between 300 and 310 nm with several resolvable vibrational features in this region, in addition to a shoulder from 350 to 400 nm of up to ~20% intensity of the maximum (see spectra of **1** as examples in Figure 4a). The absorption spectra of other Group I **PVHBOs 2**−**6** and **8** are included in the SI (Figures S3−S7 and S9).

The absorption spectra of **7**, **9**, and **10** (R = $CO_2$Me, CN, and CHO, respectively) were different from the compounds in Group I. The maximum absorption occurs around 340 nm, and the band overlaps with two other peaks at ~300 nm. Examples of absorption spectra of a Group II compound are shown in Figure 4b (**9**, R = CN). The spectra of **7** and **10** are included in the SI (Figures S8 and S10).

**PVHBOs** in Groups I and II are distinguished by their electronic transitions. The lowest-energy band in the spectrum of a Group I compound (i.e., the shoulder at 360−370 nm) is not the strongest band and therefore not the most allowed transition, which instead is the band centering at ~300 nm (see Figure 4a). The apparent lowest-energy transition of a Group II compound (~340 nm; see Figure 4b) is also the most intense band and therefore the most allowed transition. The molar absorptivities at the absorption maxima of all **PVHBOs** in all solvents (Table 1) were found within a narrow range of (3.1−3.4) × $10^4$ L/(mol cm).

**Emission.** Tables 2 and 3 report the fluorescence maxima of **PVHBOs** of the enol and keto bands, respectively. Groups I and II show contrasting emission properties. In Figure 5a, the fluorescence spectra of **1** in five solvents with varying degrees of polarity and HB basicity are included. In solvents with weak HB basicity (DCM and ACN), the emission contains only or


https://doi.org/10.1021/acs.jpca.1c10165
J. Phys. Chem. A 2022, 126, 1033−1061

Table 4. Solvent-Dependent Enol/Keto Emission Ratios (E*/K*) of PVHBOs[a]

| Comp. # | R-Group | DCM | ACN | EtOH | DMF | DMSO |
|---|---|---|---|---|---|---|
| **1** | OMe | 0 | 0.04 | 0.4 | 1.1 | 2.0 |
| **2** | Me | 0 | 0.04 | 0.4 | 1.0 | 2.1 |
| **3** | t-Bu | 0 | 0.05 | 0.4 | 1.0 | 2.0 |
| **4** | F | 0 | 0.04 | 0.4 | 0.9 | 2.2 |
| **5** | H | 0 | 0.04 | 0.5 | 1.3 | 3.2 |
| **6** | Cl | 0 | 0.04 | 0.5 | 0.8 | 1.9 |
| **7** | $CO_2CH_3$ | 0 | 0 | 0.04 | 0.07 | 0.2 |
| **8** | $CF_3$ | 0 | 0.02 | 0.3 | 0.3 | 0.9 |
| **9** | CN | 0 | 0 | 0.05 | 0.08 | 0.2 |
| **10** | CHO | 0 | 0 | ~0 | 0.03 | 0.03 |

[a]The rows of Group II compounds are shaded.

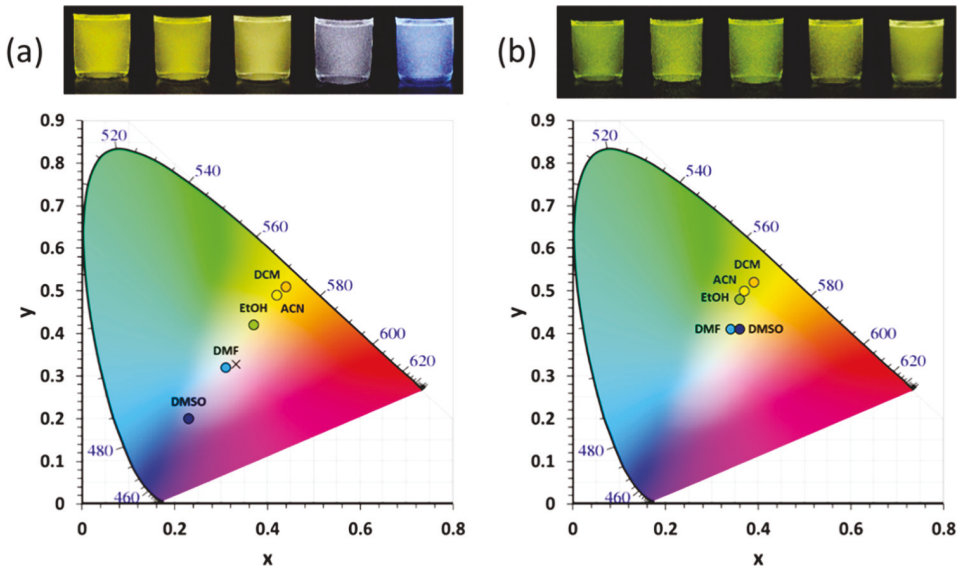


**Figure 6.** CIE 1931 color space diagrams of **1** (a) and **9** (b) in DCM (orange), ACN (yellow), EtOH (green), DMF (cyan), and DMSO (navy). [dye] = 0.5 $\mu$M. $\lambda_{ex}$ = 310 nm. The photographs of the compounds in these solvents in the above order from left to right when irradiated by a handheld UV lamp ($\lambda_{ex}$ = 365 nm) are placed on top of the CIE diagrams.

primarily the band from the keto tautomer. In solvents with higher HB basicity (DMSO, DMF, EtOH), the enol band contributes to a sizable portion of the total emission of **1**. The enol band of **1** was found at 443 nm (in DMSO) and was only observed in solvents with the capability of disrupting intramolecular HB and therefore hindering the ESIPT process. In DCM where the hydrogen-bonding capacity is absent, the enol band was not observed, and in ACN, the size of the enol band was miniscule. Similar observations were made for all compounds in Group I (Figures S11–S15 and S17).

On the other hand, compounds in Group II (**7**, **9**, and **10**) exhibit different enol vs keto emission ratios (E*/K*; Table 4) than those in Group I. Figure 5b shows the fluorescence spectra of **9** in the five solvents that were used in the


https://doi.org/10.1021/acs.jpca.1c10165
J. Phys. Chem. A 2022, 126, 1033−1061

Table 5. Average Absolute Fluorescence Quantum Yields of PVHBOs in DCM, ACN, EtOH, DMF, and DMSO[a]

| Comp. # | R-Group | DCM | ACN | EtOH | DMF | DMSO |
|---|---|---|---|---|---|---|
| **1** | OMe | 0.07 | 0.04 | 0.04 | 0.04 | 0.10 |
| **2** | Me | 0.07 | 0.03 | 0.04 | 0.06 | 0.09 |
| **3** | t-Bu | 0.07 | 0.03 | 0.04 | 0.04 | 0.10 |
| **4** | F | 0.11 | 0.03 | 0.04 | 0.04 | 0.08 |
| **5** | H | 0.06 | 0.03 | 0.04 | 0.05 | 0.11 |
| **6** | Cl | 0.10 | 0.04 | 0.05 | 0.05 | 0.09 |
| **7** | $CO_2CH_3$ | 0.14 | 0.05 | 0.06 | 0.05 | 0.06 |
| **8** | $CF_3$ | 0.11 | 0.05 | 0.05 | 0.06 | 0.05 |
| **9** | CN | 0.14 | 0.06 | 0.07 | 0.05 | 0.06 |
| **10** | CHO | 0.13 | 0.06 | 0.08 | 0.06 | 0.11 |

[a]The high values are shaded (also see the text), [dye] = 0.5 $\mu$M, $\lambda_{ex}$ = 300−390 nm, $\Delta\lambda_{ex}$ = 5 nm.

acquisition of fluorescence spectra of compounds in Group I. Spectra of **7** and **10** are in the SI (Figures S16 and S18). Unlike the unsubstituted HBO of which the enol emission is major in HB basic solvents such as DMSO and DMF,[2] the keto emission of Group II compounds is consistently dominant (Figure 5b), while the enol band remains minor even in DMSO.

Table 4 shows the enol/keto-integrated emission intensity ratios (E*/K*) determined for **PVHBO**s by fitting the normalized emission spectra with two normal distribution (Gaussian) functions. The compounds in Group II (**7**, **9**, and **10**) show low E*/K* values (up to 0.2) in all solvents. The members in Group I have a more typical solvent-dependent E*/K* trend as expected for HBO across the tested solvents from 0 in DCM up to 3.2 (of compound **5**) in DMSO. Group II compounds, which bear e-withdrawing substituents, produce strong intramolecular HBs in the ground states (see the OH chemical shifts in $CDCl_3$ in Table 1) and principally keto emission (in all solvents) in the excited states. The correlation between the electronic property of the substituent and the relative abundances of enol vs keto emission bands is similar to that of the 1-(acylamino)anthroquinones reported by Barbara and co-workers.[40,41] The explanation of the E*/K* dependence on the R substituent and solvent will be offered after the sections of the ultrafast spectroscopic and computational studies.

**Emission Colors and CIE Diagrams.** The composite emission color profiles of dual-emitting **PVHBO**s in different solvents were mapped on the CIE 1931 XYZ color space. The CIE diagram of **1** is shown in Figure 6a, with coordinates assigned for DCM (orange), ACN (yellow), EtOH (green), DMF (cyan), and DMSO (navy). The data points from DCM to DMSO track a linear line ($R^2$ > 0.99) that cuts across the region appearing white. The CIE 1931 coordinate of **1** was (0.31, 0.32) in DMF, which is close to the "ideal white" value of (0.33, 0.33). Compounds in Group I have produced similarly linear CIE color profiles that traverse the region of white color (Figures S19−S23 and S25). That is, in DMF (and in DMSO for **8**), the ($x$, $y$) coordinates of Group I members are all within 0.04−0.01 of the ideal white color (0.33, 0.33). Group II representative **9**, on the other hand, produces a profile that clusters in the green/yellow region (Figure 6b) due to the lack of contribution from the enol emission to the color profile. Compounds **7** and **10** behave similarly (Figures S24 and S26). The visual comparison of emission colors in different solvents above the CIE 1931 XYZ color spaces in Figure 6a,b, which were acquired using a handheld UV lamp for excitation ($\lambda_{ex}$ = 365 nm), directly illustrates this point.

**Fluorescence Quantum Yields.** The fluorescence quantum yields ($\phi$) of **PVHBO**s were collected in the five solvents (Table 5). The highest values (shaded in Table 5) of compounds in Group I were observed in DMSO. The primary enol emission contributed to the quantum yields of up to 0.10. In DCM, almost exclusively, the keto emission was observed. The highest quantum yields (up to 0.14) were seen in compounds with e-withdrawing R-groups (e.g., CHO, $CO_2Me$, $CF_3$, CN; shaded in Table 5). Compounds in Group II stand out from all others by possessing the three highest quantum yields of 0.14, 0.14, and 0.13 in DCM for **7**, **9**, and **10**, respectively. These values, although not adequately high for the dyes to be useful as LED emitters, are higher than that of unsubstituted HBO (∼0.02) measured under the same


https://doi.org/10.1021/acs.jpca.1c10165
J. Phys. Chem. A 2022, 126, 1033−1061

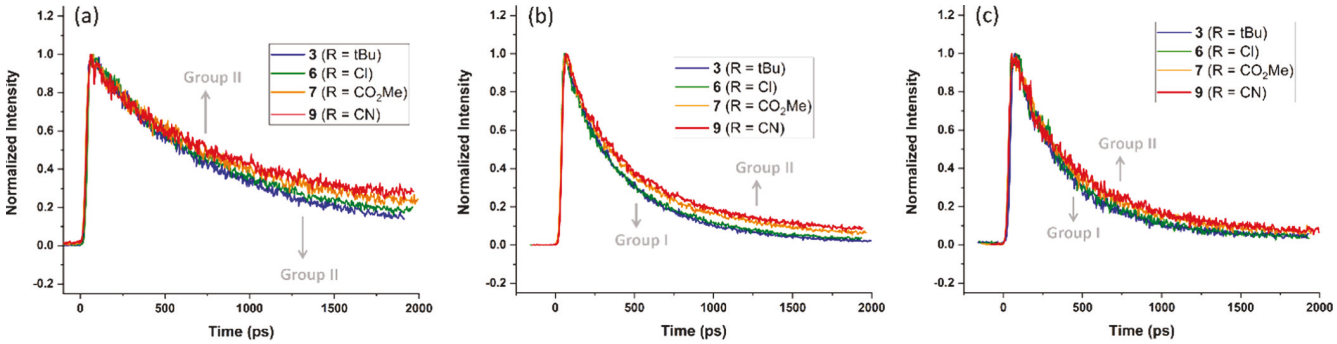


**Figure 7.** Decays of keto emission bands (570−560 nm) of **3** (blue), **6** (green), **7** (orange), and **9** (red) in (a) DCM, (b) EtOH, and (c) DMSO measured in Track 4 window.

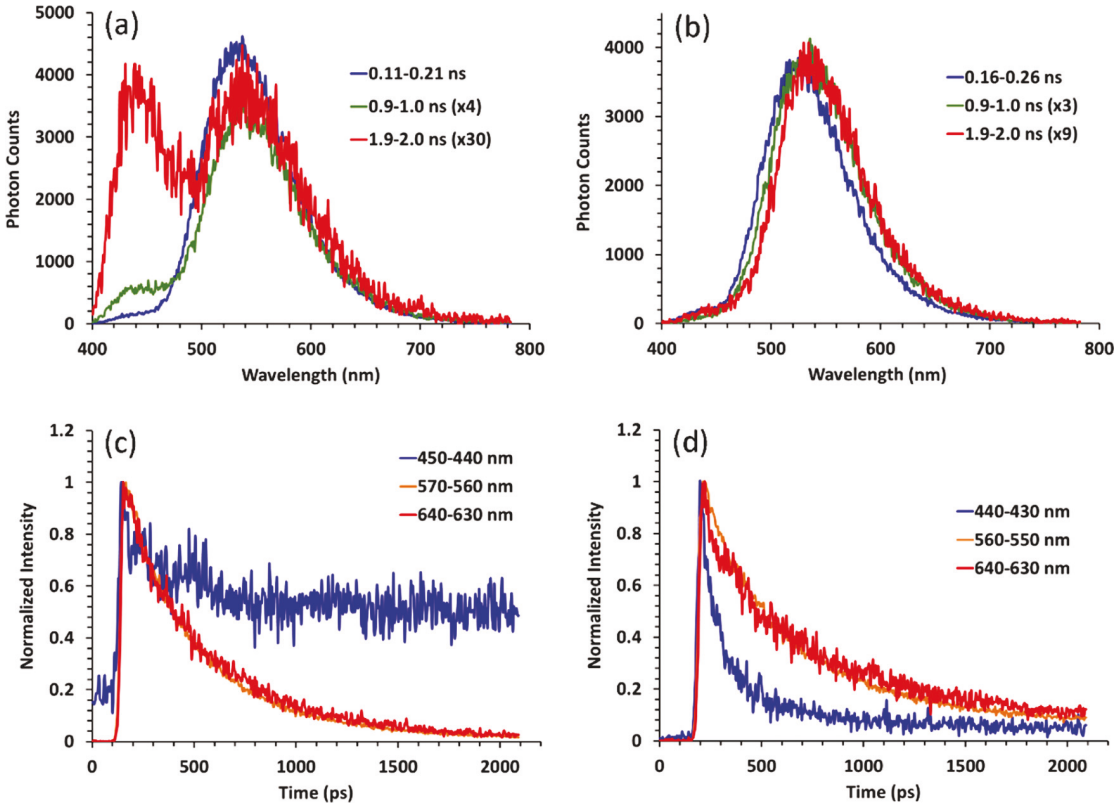


**Figure 8.** Emission spectra (a, b) and decay traces (c, d) in EtOH of **2** (R = Me, Group I, a, c) and **9** (R = CN, Group II, b, d) collected from Track 4 measurements. The major difference between **2** and **9** is seen in the 400−500 nm range. The steady-state emission spectra of **2** and **9** are shown in Figures S11 and 5b, respectively.

conditions.[2] It is therefore possible that further modifications of the ESIPT core structure may continue to elevate the emission quantum yield to open the doors to applications.

**Ultrafast Time-Resolved Emission and Absorption Spectroscopies.** The time-resolved emission and absorption data of **1**−**9** were acquired to characterize the solvent- and substituent (R)-dependent excited-state dynamics in DCM, EtOH, and DMSO. These three solvents represent those that are (1) not considered capable of hydrogen bonding (DCM), (2) both donating and accepting HB (EtOH), and (3) only accepting HB (DMSO). The transient emission experiments were done using a Hamamatsu C5680 streak camera that collects both kinetic and spectral data within different time windows. Streak camera-based time-resolved emission spectroscopy has been used to characterize emissive species involved in ESIPT processes in the picosecond time regime.[42−48] The shorter ("Track 1") of the two time windows that were applied has a 2 ps temporal resolution and covers up to 120 ps, while the longer one ("Track 4") extends to over 2 ns. The transient absorption data were acquired on an amplified Ti:sapphire laser system operating at 5 kHz with an Ultrafast Systems transient absorption spectrometer (Helios). The system has an ∼100 fs temporal resolution, which detects, spectrokinetically, both emissive and dark transient species. Emissive species can be observed in pump−probe experiments through the observation of stimulated emission (SE), e.g., an increase in probe light transmitted through the sample. Transient absorption appears as a decrease in probe light transmitted through the sample. Time-correlated single photon counting (TCSPC) experiments were also


https://doi.org/10.1021/acs.jpca.1c10165
J. Phys. Chem. A 2022, 126, 1033−1061

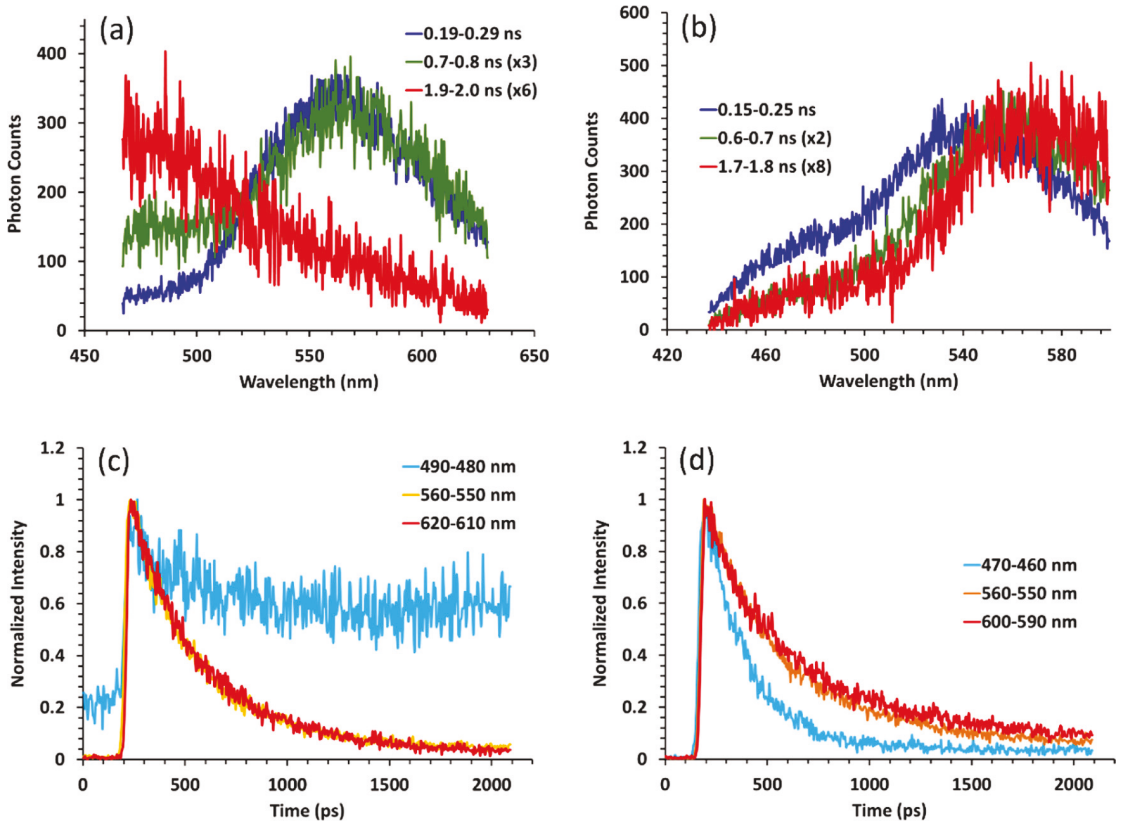


**Figure 9.** Emission spectra (a, b) and decay traces (c, d) in DMSO of **3** (R = *t*Bu, Group I, a, c) and **7** (R = $CO_2Me$, Group II, b, d) collected from Track 4 measurements. The major difference between **3** and **7** is seen in the 450−500 nm range. The steady-state emission spectra of **3** and **7** are shown in Figures S12 and S16, respectively.

carried out to complement the streak camera results, in particular, to provide higher accuracy of time constants that lay outside the Track 4 window (i.e., >2 ns). The ultrafast spectroscopic data provide (1) the emission lifetimes of the bands observed in the steady-state spectra (hundreds of ps or longer); (2) the dynamics of the short-lived emissive and dark species (tens of ps or shorter); and (3) how solvent and substituent affect the lifetimes of short- and long-lived excited-state species. Ultrafast time-resolved spectroscopies are indispensable tools in characterizing ESIPT processes, which were recently summarized in a review article by Vauthey and co-workers.[49]

*Transient Emission (TE) in DCM.* Only the emission from the post-ESIPT keto form was observed in DCM for all **PVHBO**s, which suggests that the ESIPT in DCM is too fast to be captured by this technique (the streak camera has a time resolution of ∼2 ps). Representative transient emission (TE) spectra (those of **7**) collected from both the short (Track 1) and the long (Track 4) time windows and the normalized Track 4 decay curves at three wavelength slices are shown in Figure S27. For all compounds, two rises ($t_1$ = 2−3 ps, major; $t_2$ = 10−40 ps, minor) and two decays ($t_3$ = 0.4−0.7 ns; $t_4$ = 1−5 ns) were extracted from fitting the kinetic traces collected from two separate time windows (see fitting examples in Figure S28). All of the time constant data and their amplitudes fitted from the decay data in DCM are listed in Table S1. The precisions of the two longer time constants (>100 ps) are higher than those of the two shorter time constants (<20 ps) in DCM and all other solvents. Group II compounds **7** and **9** decay slightly slower than Group I compounds (e.g., **3** and **6**), as observed in the longer (Track 4) time window (Figure 7a). There was no remarkable difference in DCM between Groups I and II compounds in the early decays of less than 120 ps (Figure S29a). As seen from the amplitude values that were measured at different wavelength slices (Tables S2 and S3), the emissions shift to longer wavelengths during Track 4 (long-time window) measurements (e.g., Figure S27b), which suggests that the spectrum of the longest $t_4$ component is on the red side of the $t_3$ component. The emission dependence on excitation wavelength is minimal in DCM (e.g., see the data of compound **7** in Table S3).

*Transient Emission in EtOH.* The emission spectra in EtOH of **2** and **9**, which represent Groups I and II compounds, respectively, at different time slices are shown in Figure 8a,b. Similar to the observations in DCM, the evolution of the keto emission contains two rises and two decays (Table S4). The longer decays ($t_4$) of the keto forms of Group II compounds **7** and **9** (and **8** with an e-withdrawing R group of $CF_3$) are larger than those of the rest (also see Figure 7b).

Unlike in DCM, the enol emission was observed in EtOH. This emission band arises within 2 ps, the temporal resolution of Track 1 measurements. The decay starts with a steep drop ($t_1$ in Table S5; also see the decay traces in Figure S30a), followed by two longer decays ($t_2$ and $t_3$ in Table S5). The rapid drop immediately following the onset of the enol emission could be assigned to solvent-involved processes such as solvent-mediated proton transfer[50] or hydrogen-bonding-assisted quenching.[51−53] The $t_2$ decays of all compounds were found to be 0.1−0.5 ns. The longest decay ($t_3$) shows a clear distinction between Groups I and II. The $t_3$ decays of all of the


https://doi.org/10.1021/acs.jpca.1c10165
J. Phys. Chem. A 2022, 126, 1033−1061

compounds in Group I are major and are too long to be fitted within the duration of these experiments (see Figure S31a, blue and green). Thus, the time constants are assigned "inf" in Table S5. Note that the $t_3$ components of a few compounds were later determined in the TCSPC experiments, which are capable of longer time-scale measurements than the streak camera. The $t_3$ components of Group II members **7** and **9** deviate from the observations on Group I compounds. The $t_3$ of compound **7** is insignificant in abundance ("inf" at 2%), while the $t_3$ of compound **9** is much shorter than those of other **PVHBO**s and minor in abundance (1.4 ns at 18%).

Consistent with the trends of decay time constants and amplitude values (Table S5), a visual examination of the TE spectra and decay traces in Figure 8 is in agreement with the conclusions that (1) the enol excited state decays much slower than the keto among Group I compounds (e.g., **2** in Figure 8a,c), (2) the opposite is true for Group II compounds (e.g., **9** in Figure 8b,d), and (3) a conversion from enol to keto was not observed. Therefore, it could be understood that the steady-state enol emission of Group I compounds in EtOH is originated from the long-lived species, while the quenching of which from Group II compounds in EtOH, as opposed to a more efficient ESIPT or an increased emission yield of the keto form, results in the dominance of the keto band in their steady-state spectra.

*Transient Emission in DMSO.* Both enol and keto emission bands of the **PVHBO** series were observed in DMSO (see examples in Figure 9a,b). The kinetic behaviors of the keto emission are similar for all **PVHBO**s (Table S6), with two rise time constants and two decays. The shorter, major rise occurs mostly at 1−3 ps, while the minor rise appears within 20−30 ps. The first keto decay ($t_3$) time constant was measured at 0.2−0.3 ns, while the second keto decay ($t_4$) was found between 1 and 2 ns and is minor. The $t_4$ components of **7** and **9** (Group II) have slightly larger abundances than the rest (see Figure 7c).

Echoing the behaviors in EtOH, Groups I and II compounds are distinguished by their enol emission kinetics in DMSO. For example, the enol band of Group I member **3** persists throughout the Track 4 window, while that of Group II member **7** rapidly declines (Figure 9c,d). During the early decays, the sharp drop of enol emission observed in EtOH is absent in DMSO (Figure S30b), suggesting that a hydrogen-bonded complex where EtOH is the HB donor could be responsible for the steep early drop of the enol emission (Figure S30a). The time constants of the evolutions of both bands are listed separately in Tables S6 (keto) and S7 (enol). The rise of the enol emission ($t_1$) in DMSO has time constants of 2−5 ps (Table S7), while the first decays ($t_2$) are mostly within 0.2−0.3 ns. The abundances of $t_2$ decays of two Group II compounds (**7** and **9**) are much larger (∼90%) than Group I compounds. Group I compounds contain a long decay ($t_3$ as "infinity") that persists beyond the experimental time window, which materializes into the enol bands of Group I compounds in the steady-state emission spectra. On the contrary, ∼90% of the decays of excited enol forms of **7** and **9** can be described by $t_2$ of 0.1−0.2 ns, while the longer $t_3$ values are short with small amplitude values. The differences in the enol decays between Groups I and II compounds measured in DMSO mirror the observations in EtOH.

*Emission Lifetime Values from the TCSPC Experiments of Selected Compounds.* The emission decay time constants of several **PVHBO**s were measured using the time-correlated single photon counting (TCSPC) method. The device that we have access to provides a lower time resolution than the previously described setup using a streak camera. The time constants longer than 150 ps are considered to be reliable, as described in the manufacturer's brochure. The benefit of the TCSPC over the earlier streak camera experiments is that the observations over a longer time frame are allowed so that the fate of the long enol decays of Group I compounds in EtOH and DMSO could be captured. The excitation source was a 296 nm LED source. The enol and keto emissions were monitored near the band maxima, e.g., 430 and 550 nm for enol and keto emissions, respectively, of compound **2** (R = Me).

The time constants and amplitude values measured using the TCSPC method are listed in Table S8. The cells of the major components of each decay are shaded in the table. In DCM (top section of Table S8) where only the keto emission could be recorded, the decay traces were fitted with two exponential terms. The shorter ones are major for Group I compounds **1** and **2**, while the opposite is true for Group II compounds **7** and **10**. The unique feature of the decays in EtOH (the middle section of Table S8) is the long components from the enol emissions of Group I compounds. For both **1** and **2**, the longer components, which are major (>50% in amplitude), are almost 7 ns. This value exceeds the observational window of 2 ns of the streak camera experiments. The decays of keto emissions in EtOH are similar to that in DCM, namely, Group I members decay faster than Group II compounds (a minor long component of keto emission was observed for each of Group I compound, which could be attributed to the crossover from the long decay of the enol emission). The bottom section of Table S8 contains the time constants and amplitudes of decays in DMSO. The difference between Groups I and II compounds in EtOH is replicated in DMSO. Specifically, the major long components of enol emission of compounds **1** and **2** are ∼8−9 ns. The lifetime of the keto emission in DCM was not altered when air ($O_2$) was purged via bubbling $N_2$ gas through the sample (Figure S32). The long components observed in EtOH show modest sensitivity toward oxygen (Figure S33), while in DMSO, the effect of oxygen is less obvious (Figure S34). No sign of triplet emission was detected. Further investigation on the modest emission quenching by $O_2$ was not pursued in this work.

The major observations from the TE experiments are summarized as follows:

a. The time evolution of the keto emission contains two short rises and two long decays, which span from ps to ns and are 1 order of magnitude apart successively from one another (e.g., Table S1). Group II compounds have slightly longer overall keto decays than Group I compounds (Figure 7).

b. The enol emission was observed in EtOH and DMSO (Figures 8 and 9). It is a minor contributor to the overall emission at the early decay times of all compounds. The behaviors of Groups I and II compounds bifurcate from that point, where the enol emission of Group I members persists beyond the duration of the streak camera measurements (2 ns), while that of Group II compounds decay quicker than the keto emission within a fraction of a nanosecond.

c. The difference in enol kinetics in EtOH and DMSO was observed in the very early phases of the decays—a rapid


https://doi.org/10.1021/acs.jpca.1c10165
J. Phys. Chem. A 2022, 126, 1033−1061

drop of intensity following the increase within the IRF in almost all compounds was seen in the former but not in the latter (Figure S30).

*Transient Absorption (TA) in DCM.* The data collected from the femtosecond time-resolved transient absorption (TA) experiments were displayed in the Surface Xplorer (SX) program (see an example in Figure 10). The pump wavelength

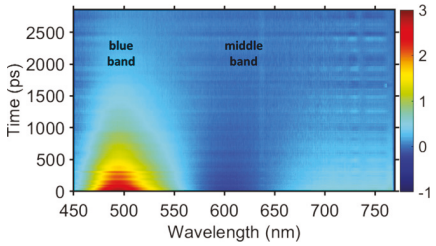


**Figure 10.** TA spectrokinetic data of **1** (R = MeO) in DCM.

was set at 310 nm, while the TA spectra were plotted between 450 and 750 nm. Because none of the **PVHBO**s absorb beyond 400 nm, the ground-state bleaching does not contribute to the TA spectra. Two major common features of the TA spectra of all nine compounds are labeled in Figure 10 as the blue band of a positive amplitude between 450 and 500 nm and the middle (of the plotted spectral region) band of a negative amplitude near 590 nm. There are other more subtle features that will be touched upon in this section and later in the Discussion section. The decay traces of the blue and middle bands were fitted using the multiexponential functions provided by the SX. The time constants and their amplitude values, fitted from the data collected in DCM, EtOH, and DMSO, are listed in Tables S9−S14. The observations of compounds **3** (R = *t*Bu) and **7** (R = $CO_2$Me) are discussed in this section as respective examples of Groups I and II members.

The TA spectra and kinetic traces measured in DCM of compounds **3** (R = *t*Bu) and **7** (R = $CO_2$Me) are shown in Figure 11a−d. The blue bands of **3** and **7** are centered at 467 nm (Figure 11a) and 460 nm (Figure 11b), respectively. The middle bands of both, which appeared after 500 fs, were found to maximize at longer wavelengths—590 and 585 nm, respectively. A notable feature is the appearance of a TA signal (a shoulder) between the blue and middle bands of compound **7**, which is absent or hidden in the TA spectra of **3**.

The kinetic response of the blue band of **3** (blue trace in Figure 11c) started with a rise of 0.37 ps ($t_1$; see Table S9), which was followed by two decays. The fitted curve is shown in Figure S35. The time constant of the minor decay is ∼70 ps ($t_2$), while the longer, major component decays at 0.9 ns ($t_3$). The kinetics of the middle band of **3** (orange trace in Figure 11c) has more features during the early stage (<20 ps) than the blue band and therefore needed more components (4) to result in a satisfactory fitting (Figure S36). The time evolution of the middle band starts with a sub-ps rise followed by an equally rapid decay. Both were fitted to the same absolute

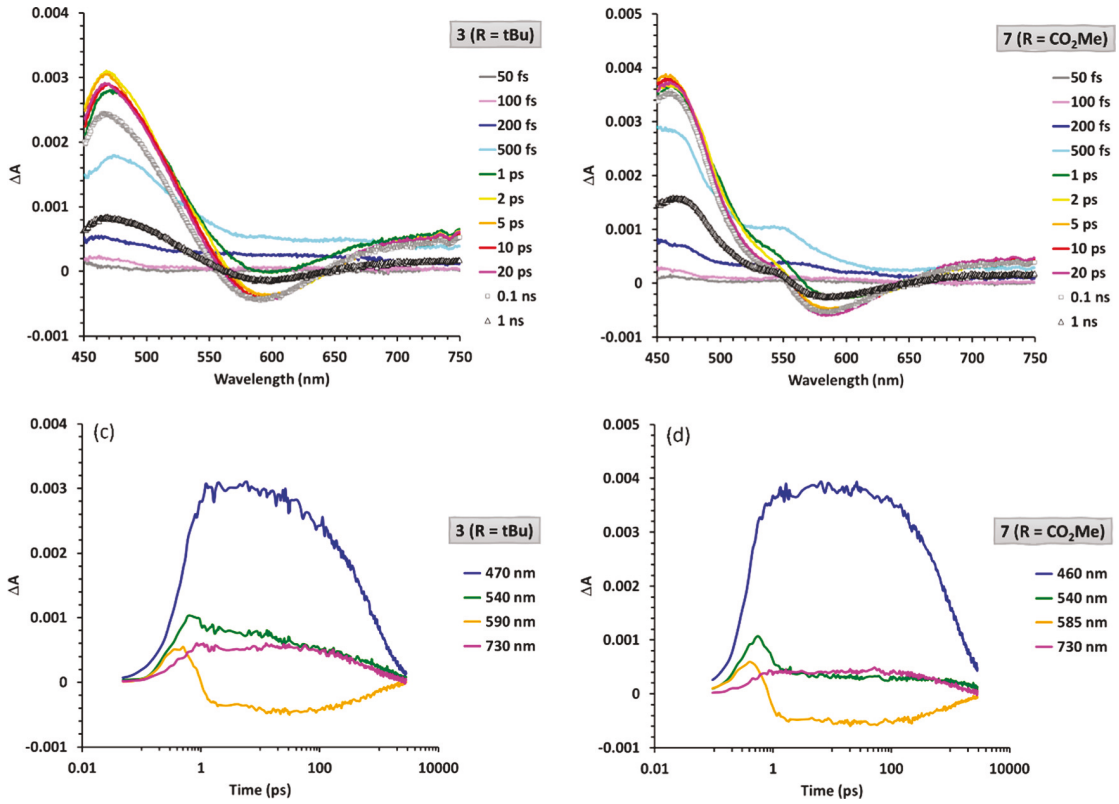


**Figure 11.** Selected transient absorption (TA) spectra (a, b) and kinetic traces (c, d) of **3** (R = *t*Bu, a, c) and **7** (R = $CO_2$Me, b, d) in DCM. Most of the TA spectra are selected from the early stage of the decays (50 fs, gray; 100 fs, violet; 200 fs, blue; 500 fs, cyan; 1 ps, green; 2 ps, yellow; 5 ps, orange; 10 ps, red; and 20 ps, magenta). The spectra taken at 0.1 ns (gray squares) and 1 ns (black triangles) are included as examples of those of the later stages of the decays. The kinetic traces (470 nm, blue; 540 nm, green; 590/585 nm, orange; and 730 nm, magenta) are plotted on a logarithmic time scale so that the features from fs to ns are discernible.



https://doi.org/10.1021/acs.jpca.1c10165
J. Phys. Chem. A 2022, 126, 1033−1061

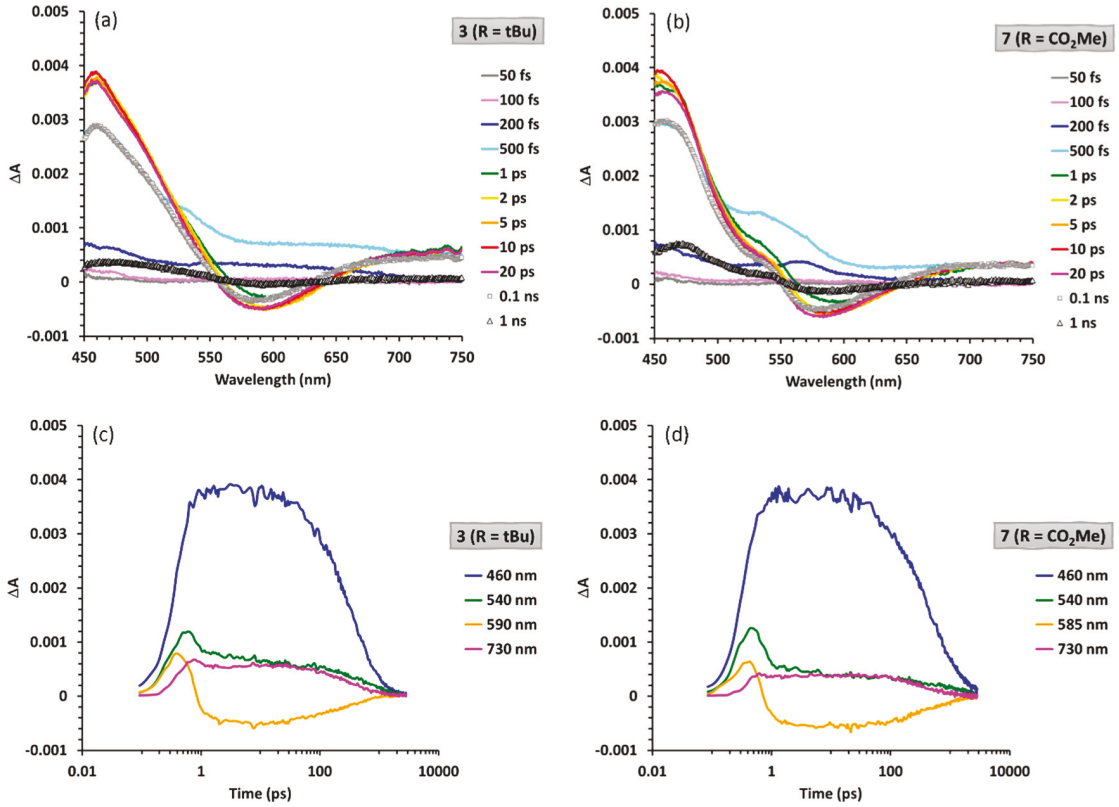


**Figure 12.** Selected transient absorption (TA) spectra (a, b) and kinetic traces (c, d) of **3** (R = *t*Bu, a, c) and **7** (R = $CO_2Me$, b, d) in EtOH. Most of the TA spectra were selected from the early stage of the decays (50 fs, gray; 100 fs, violet; 200 fs, blue; 500 fs, cyan; 1 ps, green; 2 ps, yellow; 5 ps, orange; 10 ps, red; and 20 ps, magenta). The spectra taken at 0.1 ns (gray squares) and 1 ns (black triangles) are included as examples of those of later stages of the decays. The kinetic traces (from short to long wavelengths: blue, green, orange, and magenta) are plotted on a logarithmic time scale so that the features from fs to ns are displayed.

values in time (200−300 fs) and amplitude (marked as "X" of opposite signs in Table S10). The pair of sub-ps features are followed by a minor decay of 10 ps. The longest component clocks at 0.8 ns. The sequential sub-ps rise and decay could be attributed to the production of the enol excited state (the rise, i.e., the excited-state absorption (ESA) band of the enol form) followed by an ultrafast ESIPT to produce the keto species, which results in the stimulated emission (SE)—the decay. While the SE is shifted to 590 nm, to the red of the steady-state emission peak at ∼560 nm, the red shift could be explained by the neighboring strong absorption band, which if it overlaps the SE band, it will appear to shift the maximum of the SE to the red, e.g., away from the absorption band feature. The logical extension of this analysis is the assignment of the blue band centering at 467 nm as the excited-state absorption (ESA) of the keto form after the ESIPT. The feature between the blue and middle bands in the TA spectra of **7**, which remains in the later stage of the decay (see the TA spectrum at 1 ns that are marked by black triangles in Figure 11b), can be assigned as a second ESA band of the keto form.

Fitting the decay of the blue band of Group II compound **7** (blue trace in Figure 11d) required two time constants: the rise of 0.26 ps and a decay of 1.0 ns, in addition to an "infinity" value (persisting beyond the experimental time window) with a small amplitude. Therefore, the rise of the blue band of **7** appears to be faster than Group I compounds, while the decay is slower. Similar to **3**, the decay of the middle band of **7** is described by four time constants, of which a pair of sub-ps rise and decay (0.2−0.3 ps) is followed by a low amplitude decay of 17 ps. The last time constant is 1.2 ns, which matches well with the long decay time constant of the blue band (also 1.2 ns).

The kinetic traces of other compounds in Groups I and II can be fitted similarly to those of **3** and **7**, respectively. The blue band (Table S9) of a Group II compound appears to rise faster and decay slower than that of a Group I compound. Similar observations were made for the middle band (Table S10).

*Transient Absorption in EtOH.* The two major bands (blue at ∼460 nm and middle at ∼590 nm) seen in DCM reappear in the TA spectra of samples in EtOH. The time constants (t) and amplitude values (A) obtained from multiexponential fitting are listed in Tables S11 (the blue band) and S12 (the middle band). The TA data of **3** (R = *t*Bu) and **7** (R = $CO_2Me$) are described as examples of members of Groups I and II, respectively. Selected TA spectra and kinetic traces of **3** and **7** are shown in Figure 12a−d.

The decay of the blue band of **3** (blue trace in Figure 12c) in EtOH was fitted to four time constants. In addition to a rapid rise of 220 fs and longer decays of 0.3 ns (major) and 0.8 ns (minor), which were similarly found in the decays of **3** in DCM, an extra minor rise of ∼10 ps was extracted. This component could be attributed to a solvation process, which is conceivably more significant in EtOH than in DCM. The kinetics of the middle band of **3** (orange trace in Figure 12c) requires five time constants to account for all visually discernible features. The components of ps and tens of ps have small amplitudes and large errors. Therefore, the


https://doi.org/10.1021/acs.jpca.1c10165
J. Phys. Chem. A 2022, 126, 1033−1061

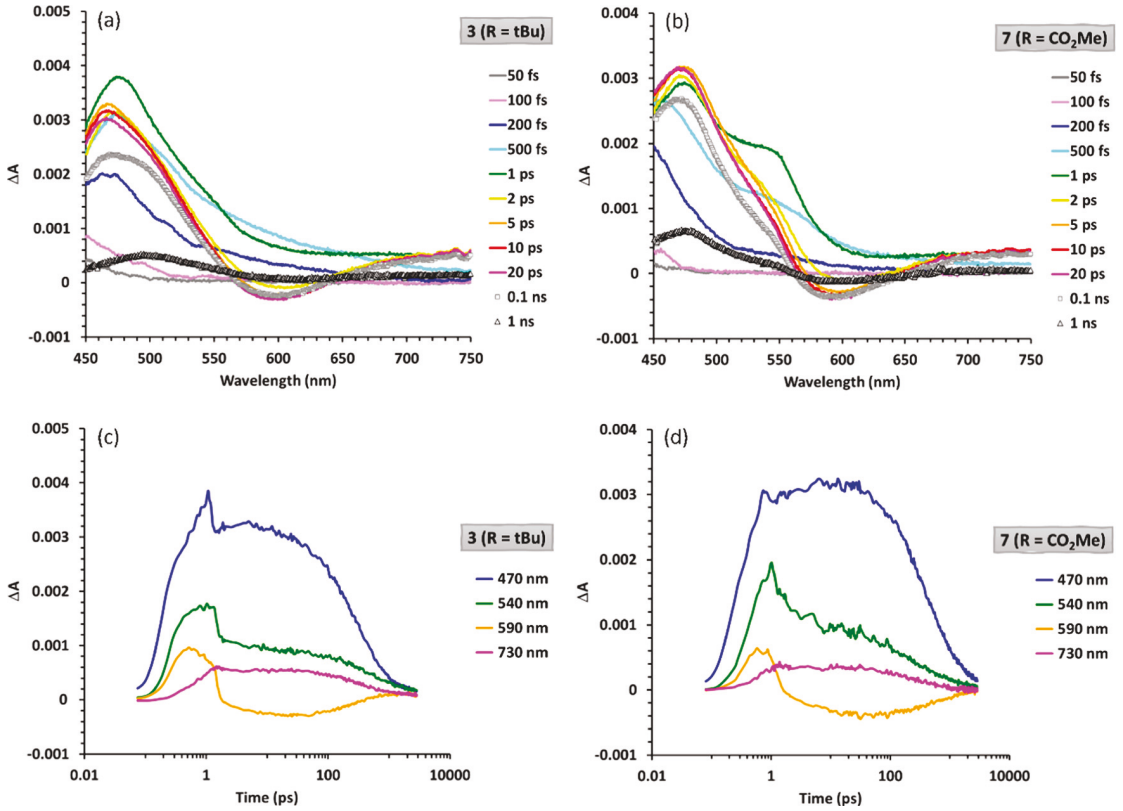


**Figure 13.** Selected transient absorption (TA) spectra (a, b) and kinetic traces (c, d) of **3** (R = *t*Bu, a, c) and **7** (R = $CO_2Me$, b, d) in DMSO. Most of the TA spectra were selected from the early stage of the decays (50 fs, gray; 100 fs, violet; 200 fs, blue; 500 fs, cyan; 1 ps, green; 2 ps, yellow; 5 ps, orange; 10 ps, red; and 20 ps, magenta). The spectra taken at 0.1 ns (gray squares) and 1 ns (black triangles) are included as examples of those of later stages of the decays. The kinetic traces (470 nm, blue; 540 nm, green; 590 nm, orange; and 730 nm, magenta) are plotted on a logarithmic time scale so that the features from fs to ns are displayed.

discussion focuses on the sub-ps features as well as the longest time constant that was fitted with the highest precision. The sequential sub-ps rise (tentatively the ESA of the enol form) and decay (the SE of the keto form) have indistinguishable time constants of 220 fs, while the longest decay component was recorded at 0.4 ns, which matches well with the $t_3$ from the blue and, presumably, the keto ESA band. The switch of the solvent from DCM to EtOH shortens the overall decay—the major component is close to 1 ns in DCM, which becomes the minor component (or altogether absent from the middle SE band) in EtOH.

The decay of the blue band (keto ESA) of Group II compound **7** (the blue trace of Figure 12d) requires four time constants for fitting. The initial rise is 210 fs, followed by a small amplitude rise of 4.5 ps, while the two long decays are 0.3 ns (major) and 1.2 ns (minor). Similar to **3**, the decay of the middle (keto SE) band of **7** is modeled by five time constants, of which the first two are rapid sub-ps rise and decay (200 fs) in succession. The last two time constants are both in hundreds of ps. The shoulder feature between the blue and middle bands that persist through the data collection, which was previously observed in DCM, again appears in the TA spectra of **7**. It is assigned as the second ESA band of the keto form.

The TA data in EtOH of other compounds were fitted similarly as done for either **3** (Group I example) or **7** (Group II). Compared with DCM, in addition to the shortening of the overall decays as mentioned earlier, the initial sub-ps rises of the blue bands, assigned to the ESA of the keto form, in EtOH are faster than those observed in DCM, suggesting that increasing solvent polarity facilitates the ESIPT. Between the two groups of compounds, the sub-ps processes of Group II compounds (**7** and **9**) are subtly but consistently faster than those of Group I compounds, while the later stages of the decays of Group II compounds are longer than those of Group I members (e.g., see Figure S37). A minor, but persistent residual amplitude ($A_{inf}$ in Table S12) was found, suggesting the presence of a species with a lifetime too long to be quantified during the experimental time window.

*Transient Absorption in DMSO.* The two major bands (blue and middle as labeled in Figure 10) seen in DCM and EtOH also appear in the TA spectra of the samples in DMSO (see Figure 13a,b). The time constants ($t$) and their amplitudes ($A$) are listed in Tables S13 (the blue band) and S14 (the middle band). Four time constants are needed to model the decay of the blue band in DMSO—sub-ps rise and decay followed by two longer decays. For Group I compounds, a positive amplitude residue has to be included for the fitting. The fittings of the sub-ps features are complicated, in addition to their indistinguishable values, by the abrupt drop of intensity at ∼1 ps observed most prominently on traces collected between 460 and 470 nm, which are not fittable using the current model (see Figure 13c, blue trace). This drop may be interpreted, however, with a low confidence, as the onset of the SE of the DMSO-solvated enol species that overlaps with the ESA band of the keto form (the blue band).

As in DCM and EtOH, the TA spectra and kinetic traces of **3** and **7** are used as examples of Groups I and II members,


https://doi.org/10.1021/acs.jpca.1c10165
J. Phys. Chem. A 2022, 126, 1033−1061

Table 6. Computed HB Lengths ($d$) in Both Vacuum and DMSO, Dihedral Angle ($|\varphi|$) between Benzoxazole and Stilbenoid in DMSO-Hydrogen-Bonded Structures, and the Equilibrium Energy ($\Delta E$ (Solvation)) between the Intramolecularly Hydrogen-Bonded and the DMSO-Hydrogen-Bonded Structures[a]

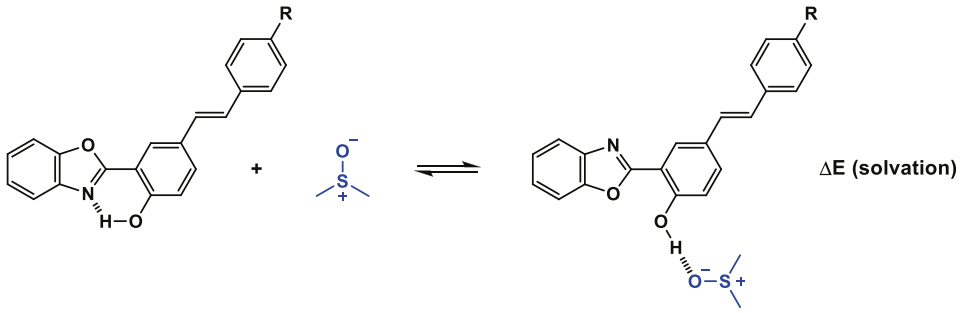


| Comp # | R | HB $(NH)_{vac}$ d (Å)[c] | HB $(NH)_{solv}$ d (Å)[d] | HB $(OH)_{solv}$ d (Å)[d] | $\|\varphi\|$ (°)[b] | ΔE solv (kcal/mol)[d] |
|---|---|---|---|---|---|---|
| **1** | MeO | 1.789 | 1.781 | 1.686 | 30 | 3.5 (2.1) |
| **2** | Me | 1.787 | 1.780 | 1.684 | 30 | 3.7 (2.2) |
| **3** | tBu | 1.787 | 1.780 | 1.684 | 30 | 3.7 (2.2) |
| **4** | F | 1.786 | 1.779 | 1.683 | 30 | 3.7 (2.0) |
| **5** | H | 1.786 | 1.779 | 1.683 | 30 | 3.7 (2.1) |
| **6** | Cl | 1.785 | 1.778 | 1.681 | 30 | 3.7 (1.9) |
| **7** | $CO_2Me$ | 1.783 | 1.777 | 1.677 | 30 | 3.7 (1.8) |
| **8** | $CF_3$ | 1.783 | 1.777 | 1.678 | 31 | 3.7 (1.7) |
| **9** | CN | 1.781 | 1.775 | 1.675 | 31 | 3.6 (1.5) |
| **10** | CHO | 1.782 | 1.776 | 1.674 | 31 | 3.6 (1.6) |

[a]DFT/B3LYP/def2-TZVP level of theory. Rows of Group II compounds are shaded. [b]Absolute values of dihedral angles ($\varphi$) between stilbenoid and benzoxazole moieties in DMSO-hydrogen-bonded **PVHBO**s. [c]Data calculated without the consideration of solvent. [d]Calculated under the COSMO model ($\varepsilon$ = 47). The values calculated without COSMO are in parentheses.

respectively. The decay of the blue band of **3** (blue trace in Figure 13c) was fitted to four time constants—a succession of the rapid rise and decay of the same value (330 fs) followed by two sub-ns (0.3 ns, major; 0.6 ns - minor) decays. It is conceivable that the sub-ps rise and decay could be attributed to the overlap of the ESA of the keto form (rise) and the SE of the DMSO-solvated enol form (decay). A long-time residual amplitude is necessary in fitting, suggesting the formation of a species that persists beyond the window of observation of the TA setup (2.8 ns).

The kinetics of the middle band of **3** (orange trace in Figure 13c; also see Table S14) starts with the sub-ps rise and decay that are fitted to the same value (490 fs). As in the previous two solvents, the pair of rapid rise and decay is assigned to the ESA of the enol and the SE of the keto species. Therefore, the fitted time constants provide the approximated values of the sub-ps ESIPT process.[54] Slower decay (18 ps) and rise (0.3 ns) follow, in addition to a long-time residual positive amplitude. The rise of 0.3 ns matches well with the $t_3$ value fitted from the blue band. Yet, the longer, minor component of 0.6 ns captured in the blue band as a decay was not detected from fitting the middle band.

The decay of the blue band of Group II member **7** (blue trace in Figure 13d) requires four time constants for fitting: sub-ps (200 fs) and ps (6.5 ps) rises and two longer decays (0.3 ns, major; 1.1 ns, minor). Therefore, the kinetic behaviors of Groups I and II compounds in DMSO are different in the early stages: the blue band of **7**, as representing Group II compounds, continues to rise prior to the two longer decays, while rapid rise and decay, the latter is likely the onset of the SE of the solvated enol, during the same time window are extracted from Group I representative **3**.

Similar to **3**, the decay of the middle band of **7** is modeled by four time constants, of which the first two are the pair of


https://doi.org/10.1021/acs.jpca.1c10165
J. Phys. Chem. A 2022, 126, 1033−1061

sub-ps rise and decay (400 fs). A 10−20 ps minor rise is extracted from the middle bands of all compounds. The longest decay constant is 0.7 ns, which is longer than the 0.3 ns registered for **3**. On the other hand, the positive residual amplitude of **7** is much smaller than that of **3**.

Two time constants are needed to fit the decays of the blue bands of all compounds in DMSO in the later stage (>100 ps; Table S13); the shorter (low hundreds of ps) of the two is more abundant than the longer (∼1 ns) one, which is the reverse order found in DCM. Compared to EtOH, the sub-ps rises are slower in DMSO. Residual positive amplitudes appear in the traces of both blue and middle bands of almost all Group I compounds (the signal-to-noise of the middle band of **1** is too low for drawing this conclusion). The values of the positive residuals of Group II compounds are significantly lower than those of Group I compounds, indicating that Group II counterparts of the persisting transient species formed from Group I compounds vanish much more rapidly. Ignoring the residual amplitudes, the overall decays of Group II compounds are slower than those of Group I compounds in DMSO (see Figure S38). Other differences between the kinetics of Groups I and II compounds in DMSO are (a) the residual amplitudes are significant only for Group I compounds; (b) for the blue bands of Group II compounds, a ps rise following the sub-ps features is required, however, not for Group I compounds (a sub-ps decay is instead used to account for the sharp drop at ∼1 ps that is more pronounced in Group I decay traces); and (c) a shoulder band, assigned to the second ESA of the keto form, between the blue (first ESA) and middle (SE) bands is seen in the TA spectra of Group II compounds but is absent or hidden in those of Group I compounds.

**Computation.** The purpose of computation is to provide a theoretical model to explain the spectroscopic observations of **PVHBO**s, which include (1) the absorption and emission wavelengths and spectral line shapes, (2) the solvent-dependent ratios of enol and keto emission bands, (3) emission quantum yields, and (4) the structural factors, both geometrical and electronic, that determine the differences between Groups I and II compounds.

The geometries are optimized on Kohn−Sham density functional theory (KS-DFT)[55,56] or the time-dependent (TD)DFT[57,58] level of theory with the B3LYP functional.[22,59] The B3LYP functional is relatively fast and is arguably the most popular functional that is applied in the DFT and (TD)DFT calculations of small organic molecules[60] including those capable of ESIPT.[61−65] The B3LYP functional also carries its limitations: (1) it may underestimate the excitation energies of the transitions with charge-transfer characters and (2) it lacks accuracy in the geometrical and energetic calculations of molecules with either large dipoles or charges. In the latter cases, range-separated hybrid functionals would be preferred,[66,67] which are not available in the tools that the authors had access to during the course of this study. Therefore, one is advised not to dwell on the numerical accuracies of the calculated vs experimental values. Rather, the relative changes that are revealed from computation as a function of a specific parameter (e.g., the substituent R) are much more valuable in contributing to a meaningful excited-state model of **PVHBO**s. All optimized structures have their secondary derivatives computed either analytically or numerically to confirm the assignments of stationary points—either a minimum or a saddle point. For all calculations except the ground-state energies in DMSO (Table 6), no solvent effect was considered. The def2-TZVP basis sets were used except for the calculations of the minimal energy paths, where the def2-SV(P) basis sets were used to keep the computational cost under control. Others have approached the ESIPT processes theoretically with different methods or from different perspectives,[65,68−73] which we may apply to selected cases in our collection of compounds in the future to understand their excited-state properties more comprehensively in the context of related works.

*Ground-State Geometries.* Selected ground-state geometrical data of **PVHBO**s are listed in Table 6, which is sorted in the ascending order of the $\sigma_p^+$ value of R. The intramolecular O−H···N HB distance decreases as the substituent R becomes more e-withdrawing. This is an indication that the HB becomes stronger, which is supported by the decrease of the calculated OH stretching frequency (Table S15). These calculations were done without the consideration of solvation.

When the COSMO model[29] was applied at the dielectric constant of DMSO ($\varepsilon$ = 47), the same trend of the strengths of both the intramolecular HB and the intermolecular version with a DMSO molecule with respect to the $\sigma_p^+$ value was observed (Table 6). The geometries of **PVHBO**s coordinated with a single DMSO solvent molecule were optimized in vacuum or with the application of COSMO. In the DMSO-hydrogen-bonded structures, the stilbenoid and HBO components are no longer coplanar. The dihedral angles over the entire series of **PVHBO**s remain remarkably constant at ∼30° (Table 6). The thermodynamic energies of the equilibrium between the intramolecularly hydrogen-bonded and the DMSO-hydrogen-bonded forms were calculated under the COSMO model. For all compounds, the endothermic solvation energy stays at 3.5−3.7 kcal/mol, insensitive to the substituent R (Table 6). The implication is that the difference in the E*/K* emission ratio (Table 4) in DMSO among all **PVHBO**s cannot be attributed to the difference in the distributions of ground-state species.

*Frontier Molecular Orbitals (FMOs) at the Ground-State Geometries.* The FMOs of **1** and **9**, which represent Groups I and II **PVHBO**s, respectively, are shown in Figure 14. The highest occupied molecular orbitals (HOMOs) of both primarily reside on the stilbenoid component. The lowest unoccupied molecular orbital (LUMO) of **1** shifts to the benzoxazole moiety, while the LUMO of **9** remains on the stilbenoid. The similar separation of HOMO and LUMO observed in Group I **PVHBO**s has been reported in other styryl-containing chromophores.[74,75] The LUMO + 1 of each compound takes up the opposite space from the LUMO. The flip of space occupancies of LUMO and LUMO + 1 as the substituent R transitions from e-donating to e-withdrawing is the principal cause of the differences in absorption and emission properties between Groups I and II compounds, as will be argued in this and the following sections.

*Ground-State Excitation Energies (i.e., UV/Vis Absorption).* The excitation energies and oscillator strengths to the $S_1$ and $S_2$ states were computed on the (TD)DFT/B3LYP level of theory (Table 7). The $S_1$ states of **1**−**6** have small oscillator strengths (0.06−0.08) and are primarily contributed from the HOMO (stilbenoid) → LUMO (HBO) transition (>88%), which is a charge-transfer transition judged by the difference in the space occupancy of the HOMO on the stilbenoid and the LUMO on the HBO component (e.g., see those of **1** in Figure 14). The $S_2$ states of **1**−**6** have much larger oscillator strengths


https://doi.org/10.1021/acs.jpca.1c10165
J. Phys. Chem. A 2022, 126, 1033−1061

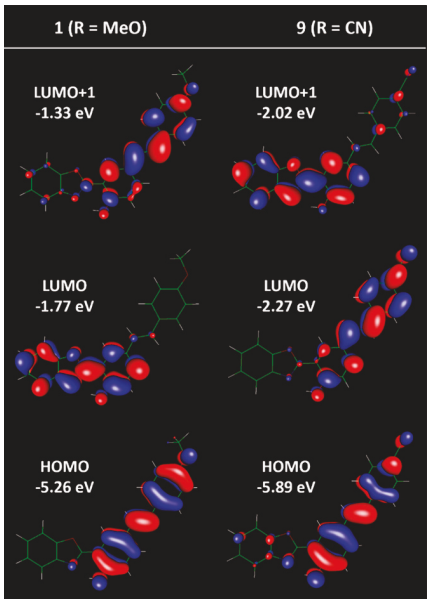


**Figure 14.** Frontier molecular orbital diagrams of **1** (left) and **9** (right) calculated at the DFT/B3LYP/def2-TZVP level of theory. The calculated orbital energy values are listed.

(1.2−1.4) because the dominant transition is HOMO → LUMO + 1 localized on the stilbenoid component.

For Group II members **7** and **9**, the space occupancies of LUMO and LUMO + 1 flip from those of Group I compounds. Consequently and counterintuitively, the major contributor to $S_1$ is HOMO (stilbenoid) → LUMO + 1 (HBO), the charge-transfer transition.[76] The allowed HOMO (stilbenoid) → LUMO (stilbenoid) transition dominates $S_2$. Because of the unusual off-order FMO contributions to the electronic transitions, the energy difference between $S_1$ and $S_2$ ($\Delta E$ in Table 7) is smaller in Group II (e.g., only 0.02 eV of **9**) than in Group I (e.g., 0.59 eV of **1**). Therefore, in the experimental absorption spectra of Group II compounds, the $S_1$ band with a small oscillator strength characteristic of charge transfer would be obscured by the closely situated, much more allowed $S_2$ band, while the absorption bands of $S_1$ and $S_2$ of Group I compounds are sufficiently separated (>0.5 eV in most cases) for a long wavelength shoulder (i.e., $S_1$) to reveal itself (Figure 4).

Compound **8** contains an e-withdrawing $CF_3$ group. However, the space occupancies of FMOs are in line with those of Group I compounds **1**−**6**, namely, with HOMO and LUMO + 1 on stilbenoid while LUMO on HBO. Both HOMO → LUMO and HOMO → LUMO + 1 transitions contribute about equally to $S_1$ and $S_2$. Therefore, compound **8** is considered a transitioning case between Groups I and II.

Compound **10**, a Group II molecule as classified based on its spectroscopic behaviors, offers up an interesting twist in the electronic structures of this series of compounds. The HOMO (stilbenoid) → LUMO (stilbenoid) transition is localized on the stilbenoid and is the major contributor to $S_1$, which differs from the charge-transfer type of $S_1$ transitions of all other molecules, and raises the oscillator strength of $S_1$ from <0.1 of

**Table 7. Calculated Two Lowest-Energy Electronic Transitions ($\lambda_1$ and $\lambda_2$ in nm), Energetic Difference Between $S_1$ and $S_2$ ($\Delta E$/eV), Oscillator Strengths ($f$), and Dominant MO Contributions at Optimized Ground-State Geometries**

| Comp. # | R | $\lambda_1$ (nm)/$f_1$ | $S_1$ dom. Contr.[a] | $\lambda_2$ (nm)/$f_2$ | $S_2$ dom. Contr.[a] | ΔE (eV) |
|---|---|---|---|---|---|---|
| **1** | MeO | 403/0.06 | H → L, 96% | 338/1.34 | H → L+1, 93% | 0.59 |
| **2** | Me | 388/0.07 | H → L, 94% | 332/1.39 | H → L+1, 92% | 0.53 |
| **3** | tBu | 388/0.07 | H → L, 94% | 335/1.45 | H → L+1, 93% | 0.50 |
| **4** | F | 381/0.08 | H → L, 92% | 331/1.18 | H → L+1, 91% | 0.50 |
| **5** | H | 381/0.08 | H → L, 92% | 330/1.23 | H → L+1, 91% | 0.51 |
| **6** | Cl | 379/0.08 | H → L, 88% | 339/1.31 | H → L+1, 87% | 0.39 |
| **7** | $CO_2Me$ | 372/0.09 | H → L+1, 70% | 360/1.31 | H → L, 72% | 0.11 |
| **8** | $CF_3$ | 366/0.11 | H → L, 56% | 343/1.17 | H → L+1, 56% | 0.22 |
| **9** | CN | 365/0.10 | H → L+1, 83% | 362/1.22 | H → L, 86% | 0.02 |
| **10** | CHO | 378/1.13 | H → L, 93% | 368/0.10 | H → L+1, 90% | 0.09 |

[a]H, HOMO; L, LUMO; L + 1, LUMO + 1; red, localization primarily on stilbenoid; blue, localization primarily on HBO.



https://doi.org/10.1021/acs.jpca.1c10165
J. Phys. Chem. A 2022, 126, 1033−1061

compounds **1**−**9** to 1.1. The $S_2$ state is primarily represented by the charge-transfer HOMO (stilbenoid) → LUMO + 1 (HBO) transition.

*Minimal Energy Proton Transfer Paths.* The minimal energy reaction paths (MEPs) of ESIPT of **1** and **9**, representing Groups I and II molecules, respectively, were calculated at the (TD)DFT/B3LYP/def2-SV(P) level of theory (Figure 15a,b). The OH distance was fixed, while all

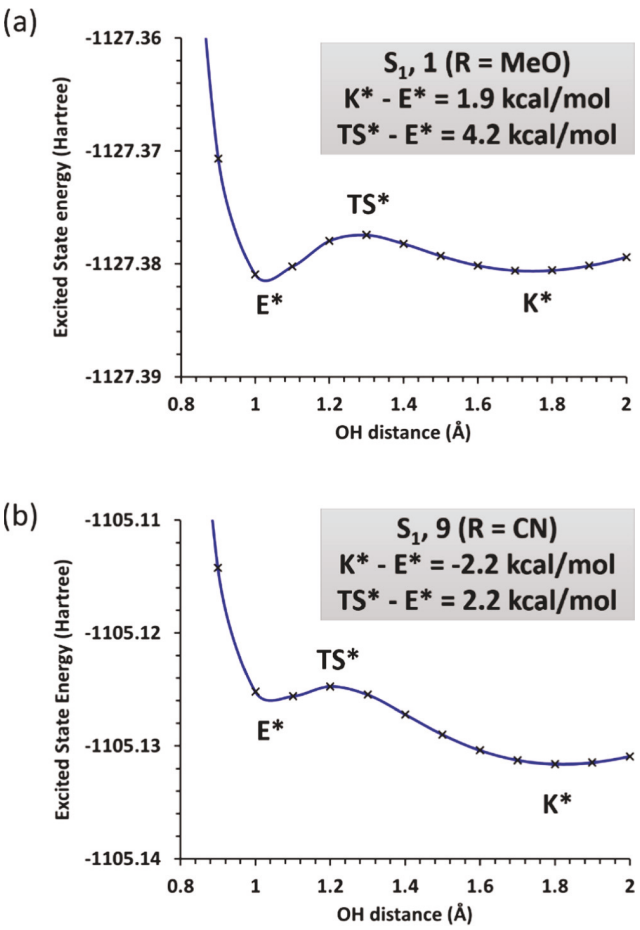


**Figure 15.** Minimal energy paths (MEPs) of **1** (a) and **9** (b) along the O−H coordinate (0.8−2.2 Å) on the first excited state ($S_1$) calculated on the (TD)DFT/B3LYP/def2-SV(P) level of theory. The energetic differences between the keto tautomer, transition state, and the enol form are noted in the insets, which were recalculated with (TD)DFT/B3LYP/def2-TZVP free of constraints.

other internal coordinates were allowed to relax in each calculation. The identified stationary points along the O−H coordinate were recalculated free of constraints using the larger def2-TZVP basis sets. The excited keto form (K*) of **1** is less stable than the excited enol (E*) by 1.9 kcal/mol (this value is dependent on the method, as will be discussed later), and the barrier along the MEP of ESIPT is 4.2 kcal/mol (Figure 15a), while the reaction energy and barrier of ESIPT of **9** are −2.2 and 2.2 kcal/mol, respectively (Figure 15b). Therefore, the keto excited state (K*) is more favored both thermodynamically and kinetically in the ESIPT reaction as the substituent R becomes more e-withdrawing (see Tables 8 and 9).

It needs to be emphasized that this conclusion was drawn by the difference of the computed results between **1** and **9**, rather than the absolute values of the calculated energies. The fact that only the keto emission of **1** was observed in a weakly polar solvent such as DCM would not be expected from a kinetic barrier of ESIPT at 4.2 kcal/mol, nor from a reaction energy that is positive at 1.9 kcal/mol (although for the sake of the argument, the emission quantum yield of the enol form could be much lower than that of the keto form). Jacquemin and co-workers opined that TDDFT tends to underestimate the energy of the excited enol in the system that they have studied.[71] Indeed, when the excitation energies were recalculated at the optimized $S_1$ geometries using a different method—the second-order coupled cluster (CC2) method—the ESIPT reaction energy values (K*−E* in Table 9) are all negative (i.e., the reactions are thermodynamically favored for all **PVHBO**s), while the correlation with the Hammett constant of the R group remains intact (i.e., a compound with a more e-withdrawing R substituent affords a more favored ESIPT reaction energy). Another point worth noting is that the calculated barrier from the minimal energy path is not necessarily the actual barrier that the reactant has to traverse for the reaction to occur. The Franck−Condon or a vibrationally hot excited enol structure might pack a whole lot more energy than the calculated minimum to elevate the reactant over the ESIPT barrier with ease.

*Excited-State Geometries and Excitation Energies of Intramolecularly Hydrogen-Bonded **PVHBO**s.* In the excited enol structures of **1**−**9**, the intramolecular N···H HB distance decreases, while the excitation energy (i.e., emission) increases as the R substituent becomes more e-withdrawing (Table 8). The emissive transition from $S_1$ carries a small oscillator strength of <0.1, with major contributions from HOMO → LUMO that is charge transfer in nature (Figure S39) except compound **9** (Figure S40), where HOMO → LUMO and HOMO → LUMO + 1 contributions are about even. The correlation of FMO contributions to the emission from the $S_1$ state tracks that of the ground-state excitation (i.e., absorption to $S_1$), and not coincidentally, the geometries of the excited- and ground-state enol forms are similar. The difference between the excited- and the ground-state enol forms is reflected in the intramolecular HB distances and dipole moments (Table 8). The N···H HB distance of the excited enol ($S_1$) is more than 0.1 Å shorter than that of the $S_0$ state, suggesting the strengthening of the HB upon electronic excitation. The dipole moment of the enol $S_1$ state is larger than the corresponding $S_0$ state, consistent with the description of charge transfer based on the FMO analysis.

In the calculated excited-state keto structures, the NH bond (Table 9), which is formed after the proton transfer, becomes shorter as the R group grows more e-withdrawing. This trend is consistent with the model that the ESIPT is more inclined to occur as the R group is more e-withdrawing, which would result in a more complete proton transfer (i.e., a shorter N−H distance) to the N of benzoxazole. When R is more e-withdrawing, which leads to the stabilization of the HOMO more so than the LUMO (data not shown), the emission wavelength decreases. The calculated emission dependence on R tracks but amplifies the experimental observations (compared to Table 3). The oscillator strength of the excitation increases when the data transition from Group I compounds (unshaded in Table 9) to Group II (shaded), which is also consistent with the experimentally measured higher emission quantum yields of Group II than Group I compounds in the least polar, intramolecular HB indifferent solvent (DCM; Table 5). The emission of any keto form can


https://doi.org/10.1021/acs.jpca.1c10165
J. Phys. Chem. A 2022, 126, 1033−1061

Table 8. Calculated HB Distances ($d$/Å), Dipole Moments ($\mu$/D), Excitation Energies ($\lambda$/nm), Oscillator Strengths ($f$), Major MO Contributions to the Enol Excited States at the Optimized $S_1$ Geometries, and the Energetic Differences between Minimized Enol (E*) and Saddle Point (TS*) Structures[a]

| Comp. # | R | NH d (Å) | μ (D) | λ (nm)/f | dom. Contr.[b] | TS*-E* (kcal/mol) |
|---|---|---|---|---|---|---|
| **1** | MeO | 1.687 | 17 | 482/0.05 | H → L, 98% | 4.2 |
| **2** | Me | 1.673 | 15 | 460/0.07 | H → L, 97% | 3.5 |
| **3** | tBu | 1.674 | 15 | 460/0.07 | H → L, 97% | 3.5 |
| **4** | F | 1.667 | 12 | 450/0.07 | H → L, 96% | 3.2 |
| **5** | H | 1.666 | 13 | 449/0.08 | H → L, 96% | 3.2 |
| **6** | Cl | 1.666 | 12 | 448/0.07 | H → L, 94% | 3.1 |
| **7** | $CO_2Me$ | 1.655 | 11 | 437/0.09 | H → L, 77% | 2.6 |
| **8** | $CF_3$ | 1.651 | 7.8 | 430/0.10 | H → L, 88% | 2.5 |
| **9** | CN | 1.647 | 5.8 | 427/0.10 | H → L+1, 54% | 2.2 |
| **10** | CHO | 1.748 | 15 | 409/1.27 | H → L, 96% | 1.7 |

[a]TDDFT/B3LYP/def2-TZVP level of theory. [b]H, HOMO; L, LUMO; L + 1, LUMO + 1; red, localization primarily on stilbenoid; and blue, localization primarily on HBO.

be almost entirely attributed to the HOMO → LUMO transition. The HOMO and LUMO plots of **1** and **9** at the optimized $S_1$ keto geometries are included in Figure S41.

The reaction energy of ESIPT of intramolecularly hydrogen-bonded conformer decreases as the R group becomes more e-withdrawing (the rightmost column in Table 9). One is advised, however, to be skeptical about the absolute calculated energy values, which are only as good as the assumptions and approximations of the method. For example, positive reaction energy values were obtained under (TD)DFT/B3LYP/def2-TZVP for several members of Group I compounds, suggesting an unfavorable ESIPT reaction in vacuum. On the contrary, almost exclusive keto emission was observed for all compounds in solvents that preserve intramolecular HBs. As briefly mentioned earlier, when a wave function-based optimization method was used (RICC2/def2-SVPD), the ESIPT reaction energies of all compounds became negative, i.e., favorable (data in parentheses in Table 9). The trend of reaction energy is still the same as the ESIPT becomes more favorable when the R group is more e-withdrawing. The comparison of these calculations cautions us against taking the absolute calculated values literally as the faithful reflection of experimental observations, regardless of the method by which they are produced. Rather, the correlation of the data with a certain physical parameter (e.g., the Hammett value of the substituent R) is meaningful in connecting the structure to chemical or spectroscopic properties.

*DMSO-Hydrogen-Bonded **PVHBOs**.* DMSO/**PVHBO** hydrogen-bonded complexes were minimized in the first excited state ($S_1$), with the aim to reveal the electronic structural factors that might have determined the difference of enol emissions between Groups I and II compounds in DMSO. A major geometrical difference between Groups I and II members in the $S_1$ is the dihedral angle between stilbenoid and benzoxazole moieties. The dihedral angles of Group I compounds, including compound **8** (R = $CF_3$), decrease from ~30 to 16−18° upon excitation from $S_0$ to $S_1$, while the impact of excitation on the dihedral angle of Group II compounds is much less (Table 10). The change of dihedral angle in response to excitation suggests the increased engagement of the benzoxazole in the $S_1$ of a DMSO-hydrogen-bonded Group I but not Group II compounds.

The FMOs of DMSO-hydrogen-bonded **1**, **8**, and **9** that contribute to the emission from the $S_1$ states are shown in Figure 16a−c. Compounds **1** and **9** represent Groups I and II compounds, respectively, while compound **8** is the transitioning member from Group I to Group II. The HOMO → LUMO transition of DMSO-hydrogen-bonded compound **1** (Figure 16a) dominates the $S_1$ emission (96%; Table 10), which can be described as a charge-transfer transition from the stilbenoid to the HBO component, and this situation is also found in the $S_1$ state of **1** in the intramolecularly hydrogen-bonded form (Figure S39). The $S_1$ emission of DMSO-hydrogen-bonded compound **9** (Figure 16c) is also dominated by the HOMO → LUMO transition, which, on the other hand,


https://doi.org/10.1021/acs.jpca.1c10165
J. Phys. Chem. A 2022, 126, 1033−1061

Table 9. Calculated HB Distances ($d$/Å), Dipole Moments ($\mu$/D), Excitation Energies ($\lambda$/nm), Oscillator Strengths ($f$), Major MO Contributions to the Keto Excited States at the Optimized $S_1$ Geometries, and the Energetic Difference between Excited Enol (E*) and Keto (K*) Forms[a]

| Comp. # | R | NH d (Å) | μ (D) | λ (nm)/f | dom. Contr.[b] | K*-E* (kcal/mol)[c] |
|---|---|---|---|---|---|---|
| **1** | MeO | 1.036 | 11 | 566/0.24 | H → L, 99% | 1.9 (-3.3) |
| **2** | Me | 1.034 | 7.9 | 547/0.27 | H → L, 99% | 0.7 (-4.0) |
| **3** | tBu | 1.033 | 8.1 | 547/0.29 | H → L, 99% | 0.7 (-4.0) |
| **4** | F | 1.033 | 5.0 | 538/0.28 | H → L, 99% | 0.1 (-4.6) |
| **5** | H | 1.033 | 6.2 | 538/0.28 | H → L, 99% | 0.05 (-4.4) |
| **6** | Cl | 1.032 | 4.6 | 537/0.30 | H → L, 98% | -0.2 (-4.9) |
| **7** | $CO_2Me$ | 1.030 | 3.2 | 530/0.38 | H → L, 98% | -1.2 (-5.3) |
| **8** | $CF_3$ | 1.029 | 1.5 | 522/0.34 | H → L, 98% | -1.6 (-5.6) |
| **9** | CN | 1.028 | 2.8 | 521/0.40 | H → L, 98% | -2.2 (-6.0) |
| **10** | CHO | 1.029 | 3.5 | 526/0.43 | H → L, 97% | -2.5 (-7.2) |

[a]TDDFT/B3LYP/def2-TZVP level of theory. [b]H, HOMO; L, LUMO. [c]Calculated values from the optimized geometries at the RICC2/def2-SVPD level of theory are in parentheses.

localizes on the stilbenoid moiety. The $S_1$ state of the nonsolvated, intramolecularly hydrogen-bonded **9**, however, is principally contributed by its HOMO → LUMO + 1 transition that carries a significant degree of charge-transfer character (Figure S40).

The major geometrical difference among these three excited, DMSO-hydrogen-bonded complexes is the length of the HBs, which are ∼0.1 Å shorter in the complexes of Group II members **7** and **9** than found in Group I compound **1** (Table 10). Meanwhile, the lengths of these intermolecular HBs are much shorter in the $S_1$ state than in the ground state in Group II but not nearly as much in Group I, **PVHBO**/DMSO complexes (see $\Delta HB_{(XS-GS)}$ values in Table 10). The FMO differences at the $S_1$ geometries result in the difference in the oscillator strengths (f) of the emission—DMSO-hydrogen-bonded **1** has a low value of f (0.04) due to the poor overlap of FMOs, while the f value of DMSO-hydrogen-bonded **9** is high (1.28).

The $S_1$ emission of compound **8** when hydrogen bonded with a DMSO molecule involves contributions from both HOMO → LUMO (66%) and HOMO → LUMO + 1 (30%). Both transitions have strong charge-transfer characters because both LUMO and LUMO + 1 extend to the HBO component (Figure 16b), while the HOMO stays on the stilbenoid. Therefore, the $f$ values of the emission of **8**/DMSO complex are low (0.07), and the HB in the $S_1$ state of **8**/DMSO complex is not as short as those found in Group II members **7** and **9**. These findings are consistent with the experimental observation that the solvent-dependent emission of **8** is similar to that of Group I rather than that of Group II (Figure S17).

## DISCUSSION

One of the interesting discoveries in this work is the clean break of the absorption and solvent-dependent emission properties between Groups I and II **PVHBO**s. As remarked in the Ground-State Excitation Energies (i.e., UV/Vis Absorption) section, the features of the absorption spectra of **PVHBO**s could be understood by the substituent-dependent FMO contributions to the first two lowest electronic transitions (i.e., $S_1$ and $S_2$). In the Discussion section, the trend of enol vs keto (E*/K*) emission ratio in the **PVHBO** series is explained, followed by the introduction of a mechanistic model that summarizes the major solvent- and R-dependent excited-state pathways leading to the emissions of **PVHBO**s.

**Solvent- and Substituent-Dependent Ratios of Enol vs Keto Emission.** Keto emissions of all **PVHBO**s dominate in DCM. In EtOH and DMSO, Group I compounds afford much more enol emission than Group II compounds. How the emissions of the two groups of compounds respond differently to a hydrogen-bonding solvent could be explained with any of the following hypotheses: (1) the ESIPT of Group II compounds are more complete than Group I compounds; (2) a larger proportion of solvated (i.e., solvent-hydrogen-bonded) species, which would afford the enol emission, could be found for Group I compounds than for Group II in the


https://doi.org/10.1021/acs.jpca.1c10165
J. Phys. Chem. A 2022, 126, 1033−1061

**Table 10. Calculated (TDDFT/B3LYP/def2-TZVP) Geometrical and Spectroscopic Properties of DMSO-Hydrogen-Bonded PVHBOs in the $S_1$ State**

| Comp. # | R | $OH_{GS}$ (HB) /Å[a] | $OH_{XS}$ (HB)/Å[b] | $\Delta HB_{(XS-GS)}$/Å | \|φ\| (°) | $\lambda_{em}$/nm | f | $\mu_{XS}$ (D) | Dom. Contr.[c] |
|---|---|---|---|---|---|---|---|---|---|
| **1** | OMe | 1.81 | 1.85 | 0.04 | 16 | 464 | 0.04 | 14 | H → L, 96% |
| **2** | Me | 1.81 | 1.81 | 0 | 17 | 445 | 0.05 | 10 | H → L, 93% |
| **3** | tBu | 1.81 | 1.82 | 0.01 | 17 | 445 | 0.05 | 10 | H → L, 93% |
| **4** | F | 1.80 | 1.80 | 0 | 17 | 436 | 0.06 | 7 | H → L, 91% |
| **5** | H | 1.80 | 1.79 | -0.01 | 17 | 436 | 0.06 | 8 | H → L, 91% |
| **6** | Cl | 1.80 | 1.79 | -0.01 | 17 | 433 | 0.06 | 7 | H → L, 86% |
| **7** | $CO_2Me$ | 1.79 | 1.72 | -0.07 | 29 | 406 | 1.31 | 15 | H → L, 98% |
| **8** | $CF_3$ | 1.79 | 1.76 | -0.03 | 18 | 416 | 0.07 | 5 | H → L, 66% |
| **9** | CN | 1.79 | 1.72 | -0.07 | 28 | 404 | 1.28 | 20 | H → L, 98% |
| **10** | CHO | 1.79 | 1.71 | -0.08 | 25 | 415 | 1.22 | 22 | H → L, 97% |

[a]GS: ground state $S_0$. [b]XS: excited state $S_1$. [c]H, HOMO; L, LUMO; red, primary localization on stilbenoid; blue, primary localization on HBO; and green, delocalization over both stilbenoid and HBO.

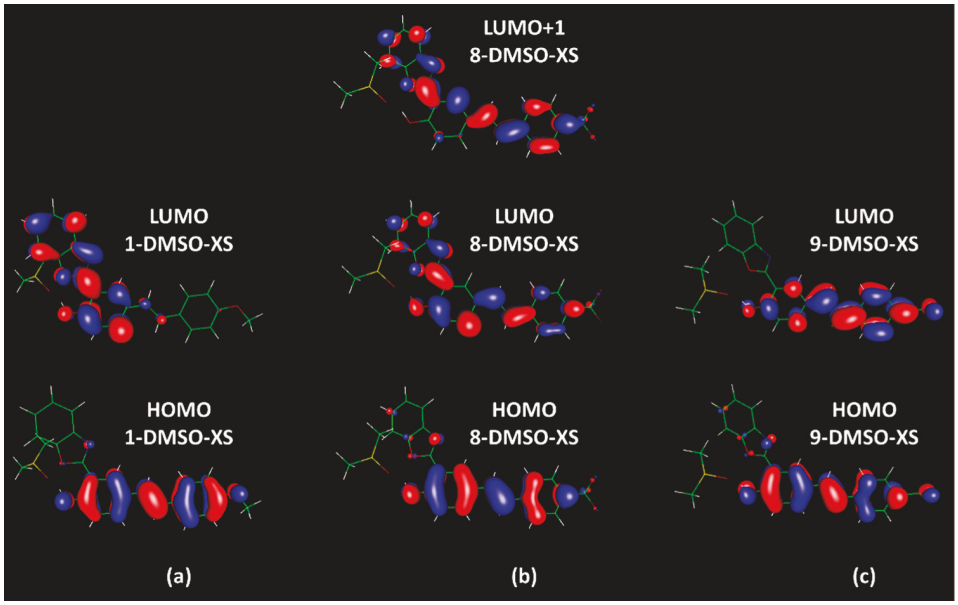


**Figure 16.** FMOs of DMSO-hydrogen-bonded **1**, **8**, and **9** that are involved in the emissive states at relaxed $S_1$ (XS) geometries computed under the (TD)DFT/B3LYP/def2-TZVP level of theory.

ground state; (3) the keto isomers of Group II compounds are brighter than those of Group I compounds in a hydrogen-bonding solvent; and (4) the enol isomers of Group II compounds are quenched to a greater degree than those of Group I compounds in a hydrogen-bonding solvent. With the information extracted from time-resolved spectroscopies and computation, the veracity of these hypotheses can be assessed.

Hypothesis #1 could be supported by the calculated dependence of the reaction energy of ESIPT on the substituent R (Table 9). A shorter N···H distance of a Group II compound


https://doi.org/10.1021/acs.jpca.1c10165
J. Phys. Chem. A 2022, 126, 1033−1061

Scheme 2. Model of Solvent (DCM and DMSO)- and Substituent (R)-Dependent Dual Emissions of PVHBOs[a]

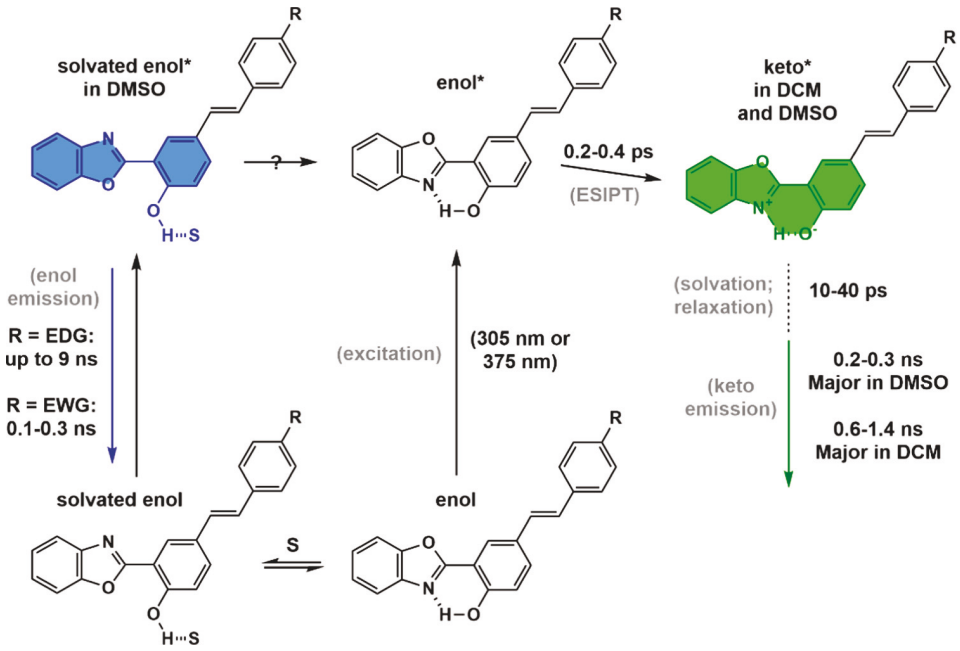


[a]The emissive species are marked by matching colors in the portions that their LUMOs occupy.

than that in a Group I **PVHBO** in the ground state (Table 6) would also lead to a more efficient ESIPT because the displaced H would travel less distance from O to N. As concluded from both calculations, the propensity of ESIPT increases as the R group becomes more e-withdrawing, which is consistent with a lower E*/K* ratio as the R group is trending up on the Hammett scale. This rationale was used to explain the varying normal/tautomer emission ratio of substituted 1-(acylamino)anthraquinones.[41] Based on the femtosecond transient absorption (fsTA) data of **PVHBO**s, the rises of the keto ESA and SE of Group II compounds are slightly but consistently faster than Group I compounds. However, the reaction energies in Table 9 were calculated on the intramolecularly hydrogen-bonded species, which based on the emission spectra in DCM afford almost exclusively the keto emission irrespective of R (Table 4). Therefore, although all of the time-resolved spectroscopic and computational data support the conclusion that Group II compounds are more inclined to undergo ESIPT than Group I compounds, they are irrelevant to the understanding of E*/K* ratio, which is 0 for all **PVHBO**s in DCM that is most closely mimicked in computation. The interpretation of the trend of the E*/K* ratio, therefore, needs to involve the solvent in which the enol emission was observed.

The ground-state equilibrium between the intact and the solvated (i.e., hydrogen-bonded with DMSO) molecules was not found to be affected by the R group based on the calculated data when the general solvent effect was considered using the COSMO model (Table 6). When the implicit solvation was not taken into account, the explicit solvation (i.e., via hydrogen bonding) of a **PVHBO** by DMSO was shown to be slightly favored as the R becomes more e-withdrawing (Table 6). The results from both calculations would negate Hypothesis #2. The solvent-dependent E*/K* ratio of each **PVHBO** therefore has to be determined by the fates of the solvent-hydrogen-bonded (affording the enol emission) vs intramolecularly hydrogen-bonded (affording the keto emission) species in the excited state.

The calculated oscillator strengths ($f$ values) of intramolecularly hydrogen-bonded keto forms in the $S_1$ states are higher in Group II than in Group I compounds (Table 9), which does not contradict Hypothesis #3. The calculated f values of DMSO-hydrogen-bonded excited enol species of **7** and **9** are very large (>1; see Table 10). Yet, the enol emissions of both are only minor relative to their keto emissions (Table 4). Therefore, the f value alone is evidently not a good indicator of fluorescence quantum yield ($\phi$), which is determined by the rates of both radiative ($k_r$) and nonradiative ($k_{nr}$) decays (eq 1). Only the $k_r$ scales with the $f$ value, while the $k_{nr}$ would come from a number of processes, including notably how the excited state interacts with the surrounding solvent molecules

$$\phi = \frac{k_r}{k_r + k_{nr}} \quad (1)$$

Based on the time-resolved emission data, the enol emissions of Group II compounds (e.g., **9**) are quickly quenched in EtOH or DMSO, while the enol emissions of Group I compounds (e.g., **2**) persist for much longer (Figures 8 and 9). The quenching of the enol emissions of Group II compounds could be attributed to the tightening of the HBs in their excited-state DMSO complexes (see data of **7** and **9** in Table 10) that are shorter than the typical Group I compound **1** by ~0.1 Å. The strong (or stronger than those in the $S_0$) HBs help dissipate the electronic excitation energy to the surrounding solvent molecules and hence facilitate internal conversion.[51,53,77−79] The large dipole moments of DMSO-hydrogen-bonded Group II enol forms (e.g., $\mu_{XS}$ of **7** and **9** in Table 10) in the excited state would lead to further engagement with solvent molecules and therefore to contribute to the same outcome. The $k_{nr}$ values of the DMSO-hydrogen-bonded **7** and **9** therefore could be tremendous (Hypothesis #4), which


https://doi.org/10.1021/acs.jpca.1c10165
J. Phys. Chem. A 2022, 126, 1033−1061

would drive down the fluorescence quantum yields (eq 1) of their enol species.

**Emission in DCM.** Similar to other ESIPT compounds,[31,49,54,80,81] a number of processes may transpire after the liftoff of a **PVHBO** to the excited state and before its return to the ground state. Vibrational relaxation, internal conversion, excited-state intramolecular proton transfer (ESIPT), solvent relaxation, and emission are most certain to occur. Charge-transfer, conformational change, and trans−cis photoisomerization are likely. Based on the experimental and computational evidence, as well as the accumulated knowledge of similar compounds in the literature, we could project some, but not all, processes on an excited-state model of **PVHBO**s, which is shown in Scheme 2.

Of all of the **PVHBO** compounds, only the keto emission was observed in DCM. DCM would not disrupt an intramolecular HB. The O−H···N bond is overwhelmingly favored over the O−H···O bond in a HBO framework.[19] Therefore, the vast majority of the ensemble of any given **PVHBO** in DCM contains the intramolecular O−H···N HB that would lead to the ESIPT. Based on the chemical shift values of OH (Table 1) and calculated HB distances (Table 6), Group II compounds contain stronger intramolecular HBs and would undergo more rapid ESIPT processes, which is consistent with the data from fsTA experiments. The geometry optimizations of both enol and keto structures on the $S_1$ surfaces confirm the thermodynamic and kinetic favorability of Group II compounds to undergo ESIPT over Group I compounds (Tables 8 and 9). Yet, the ESIPT trend found in computation is masked experimentally in DCM by the utter domination of the keto emission.

ESIPT and solvent relaxation are two major (sub)-picosecond processes during the decays of the excited singlets of ESIPT-capable molecules. Depending on the molecular structure and medium, ESIPT have been measured at tens of fs[8,54,82−88] or in the regime of hundreds of fs,[11,41,81] which is still considered shorter than solvent relaxation.[40] One may also find ESIPT processes that were measured in the ps regime that are in lockstep with solvent reorganization[14,89] or even longer.[46,48] In the current study, the transient emission (TE) data show that the keto emission of a **PVHBO** rises within 2−3 ps, the time resolution of the instrument, implying that ESIPT are completed within that time frame. From the transient absorption (TA) data, the rise of the blue band is complete at ∼1 ps, while the middle band is fully formed. The fitted time constant of this process from the TA data is 300−400 fs, which ought to be the ESIPT,[81] and in consequence, the blue and middle bands are assigned as the ESA and SE, respectively, of the keto form. The time constants of ESIPT of **PVHBO**s are larger than that of unsubstituted HBO (150 fs),[11] which is consistent with the fact that the calculated reaction (1.9 to −2.5 kcal/mol for **PVHBO**s; −5.6 kcal/mol for HBO) and barrier (4.2−1.7 kcal/mol for **PVHBO**s; 0.8 for HBO) energy values (TDDFT/B3LYP/def2-TZVP) both suggest a more rapid ESIPT of HBO[19] than the series of **PVHBO**s.

A minor slower rise of tens of ps in the TE kinetics was also observed for all compounds, which can be attributed to a solvent relaxation process.[90] This time window falls at the slow end of the reported ranges of solvent-assisted relaxation.[43,48] During that period, a small blue shift of emission was observed (e.g., **7** in Figure S27a), which suggests that the excited keto form moves to a geometry that slightly favors the ground state, i.e., the slope of the potential energy surface of the ground state is steeper than that of the excited state around the region of the keto geometry. This interpretation was drawn based on the observation of the vibrational cooling of HBO by Wang et al.[11] and from a report by Takeuchi and Tahara on a similar vibrational cooling-actuated blue shift of the excited state of an ESIPT system.[54] A blue shift of the same origin is discernible in the middle SE band of **7** (Figure 11b). The last two longer TE decays suggest that more than one emissive species is available to the keto tautomer. The amplitude of the longest decay becomes larger when fitted at longer emission wavelengths (Table S2), suggesting that the emissive species with the lower excitation energy also has a longer lifetime. The increase of overall lifetime upon increasing the emission wavelength at which the decay is recorded was reported for stilbenoid-containing dyes by Gordon and co-workers,[75] which, by conjecture, could be attributed to the concurrent solvent reorganization during emission,[75] ground-state conformational heterogeneity,[31] or the formation of a transient photoisomeric emissive species.[91]

**Emission in DMSO.** The TE spectra of the keto forms of Groups I and II compounds in DMSO are similar to those found in DCM and similar to one another. The emitter in both solvents should be the intramolecularly hydrogen-bonded, ESIPT product keto tautomer, which is relatively insulated from specific solvent interactions. Two long (>100 ps) emission decays are identified, while the shorter of which has a larger amplitude than the longer one. The relative magnitudes of the amplitude values of these two keto emission decays are of the opposite order from those in DCM, suggesting that the emissive species with a longer time constant is quenched more efficiently in a more polar solvent, likely because it carries a more charge-transfer character (hence longer excited-state lifetime).

The enol emission found in the TE data shows the most remarkable difference between Groups I and II compounds. Enol emissions of Group I members persist throughout the experimental time window (>2 ns), while those of Group II members decay within the first 200 ps. Therefore, the domination of the keto emission of a Group II compound is attributed to a highly effective quenching of enol emission rather than an increased efficiency of keto emission as the R group becomes more e-withdrawing. The TA data show that both blue (keto ESA) and middle (keto SE) bands decay with a major component at ∼0.3 ns. Both blue and middle bands in the TA spectra of Group I compounds have to be fitted with an "infinity" time constant with a significant amplitude, suggesting that the ESA of the solvated enol, which shall persist as deduced from the TE data, overlaps with both the ESA and the SE of the keto form.

In DMSO, a significant portion of the emission of any Group I compound is from the excited enol, while the keto band dominates the emission of Group II compounds. It is tempting to cite the predisposition of Group II compounds (Table 9) to undergo ESIPT to explain the difference. However, this argument would have also worked for the observations in DCM but does not. Furthermore, the enol and keto emissions do not exhibit a precursor−successor relationship in the time-resolved emission experiments (e.g., Figure 9c), suggesting that the two bands originated from two different ground-state species—the DMSO-hydrogen-bonded, which results in the enol emission, and the intramolecularly hydrogen-bonded that is transformed to the excited tautomer


https://doi.org/10.1021/acs.jpca.1c10165
J. Phys. Chem. A 2022, 126, 1033−1061

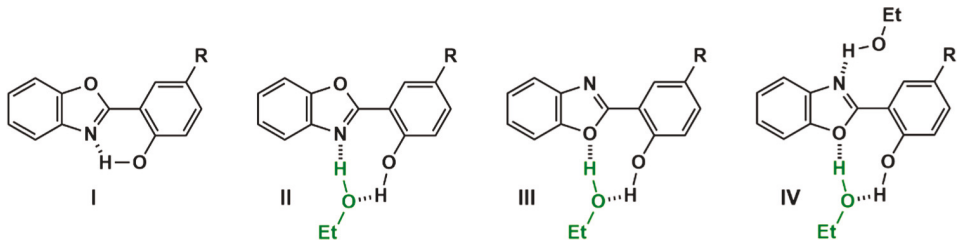


**Figure 17.** Few postulated hydrogen-bonded species in EtOH. **I** and **II** would lead to the keto tautomer via proton transfer, which **III** and **IV** would not.

and in consequence results in the keto emission (a similar lack of kinetic correlation between enol and keto emissions of unsubstituted HBO in a polar solvent was observed in the past, which, different from our interpretation of **PVHBO**s, was attributed to the two intramolecularly hydrogen-bonded conformers of HBO that are not interconverting in the excited state[9]). The ground-state solvation equilibrium was studied computationally and was concluded to yield similar equilibrium energy across all compounds (Table 6). Therefore, the difference between Groups I and II has to be determined by the excited-state properties of the solvent-hydrogen-bonded species vs the intramolecularly hydrogen-bonded ESIPT precursor. The assignments of enol and keto emissions to the solvent-hydrogen-bonded and the intramolecularly hydrogen-bonded species, respectively, without an excited-state interconversion in the cohort of ESIPT-capable molecules are precedented. Examples include 2-hydroxy-4,5-naphthotropone[42] and 2-(2′-hydroxyphenyl)-imidazo[1,2-*a*]pyridine,[92] the dual emissions of which in hydrogen-bonding solvents are attributed to the solvent-bound and the intramolecularly hydrogen-bonded populations.

**Emission in EtOH.** The difference of the E*/K* ratio between Groups I and II compounds that was observed in DMSO is replicated in EtOH, in which Group I compounds afford a sizable amount of enol emission, while Group II compounds have little of that. The kinetic model leading to the emission properties of **PVHBO** in EtOH similar to that in DMSO is therefore not reiterated. There is no equilibrium between the excited keto and enol forms based on the emission decay time constants measured using either a streak camera or with the TCSPC method. Rather, the keto and enol emissions can be attributed to the intramolecularly hydrogen-bonded and the EtOH-hydrongen-bonded forms, **I** and perhaps **III** in Figure 17, respectively. Unlike DMSO, EtOH could enable a proton transfer relay in a monosolvate of **PVHBO** (**II** in Figure 17) to afford a keto tautomer, which has been reported in similar compounds.[50,52,93−95] This process may account for the sharp loss of intensity in the first few ps of the enol emission (Figure S30a).[96] The engagement of the monosolvate in ESIPT and the lack thereof of the disolvate of 3-hydroxyflavone in an alcohol was described by Kelley and co-workers.[96] The emission quantum yields of **PVHBO**s in EtOH are generally lower than those measured in DMSO, attributable to the more effective dissipation of excitation energy to solvent in EtOH[97,98] than in DMSO via, for instance, the formation of n:1 EtOH/**PVHBO** complexes (e.g., **IV** in Figure 17).[50,94] A population of Group I EtOH-hydrogen-bonded enol species may decay slowly from a charge-transfer excited state similar to those found in DMSO to account for the long-time constants of enol emissions in EtOH of Group I compounds, while the $S_1$ states of enol species of Group II compounds could be quenched via strong hydrogen bonding with the surrounding solvent molecules.

**Substituent R and Solvent Determine the Localizations of LUMO and LUMO + 1 of PVHBOs.** The solvent-dependent E*/K* emission ratio between Groups I and II **PVHBO**s can be connected to the relative energies of the unoccupied molecular orbitals residing on the stilbenoid or the HBO component. Of all **PVHBO**s at the optimized ground-state geometries that contain an intramolecular HB, HOMO resides on the stilbenoid component (Figure 18a). In Group I

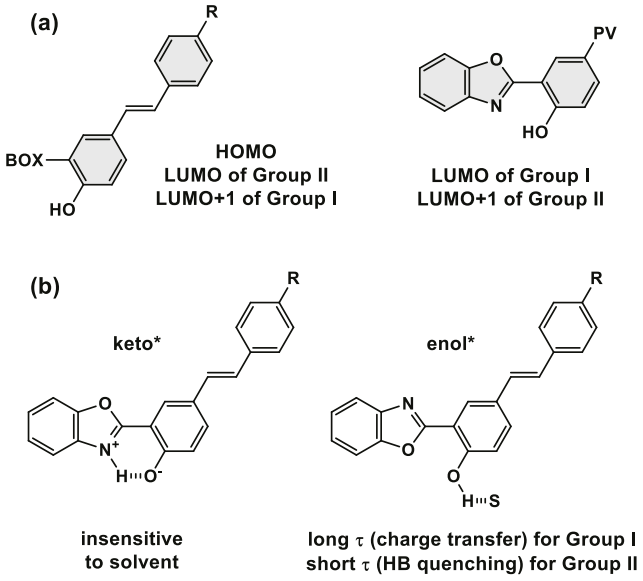


**Figure 18.** (a) FMO occupation of **PVHBO**s based on calculations of the ground states. **BOX**: benzoxazole; **PV**: phenylenevinylene. (b) Two emissive species of **PVHBO**s.

compounds, the LUMO is on the HBO while LUMO + 1 is on the stilbenoid, while in Group II compounds, the LUMO and LUMO + 1 spatial occupations are flipped (Figure 18a). The localization preferences of LUMO and LUMO + 1 are impacted by either electronic level (whether it is $S_0$ or $S_1$) or solvent-hydrogen bonding, and the sensitivity to the impact is maximized at Groups I and II boundaries (compounds **7** and **8**). For example, the LUMO of **7** (R = $CO_2Me$) is found primarily on the stilbenoid in the $S_0$, while the occupation of LUMO shifts toward the HBO in the $S_1$ (Figure S42). In DMSO-hydrogen-bonded **PVHBO**s, both LUMO and LUMO + 1 of Group I compounds become more delocalized over both the stilbenoid and the HBO when visualized at the $S_0$ geometries (e.g., see LUMO and LUMO + 1 of compound **5** in Figure S43).


https://doi.org/10.1021/acs.jpca.1c10165
J. Phys. Chem. A 2022, 126, 1033−1061

As the R group becomes more e-withdrawing (represented by the order of violet/blue to red/magenta in Figure 19), the

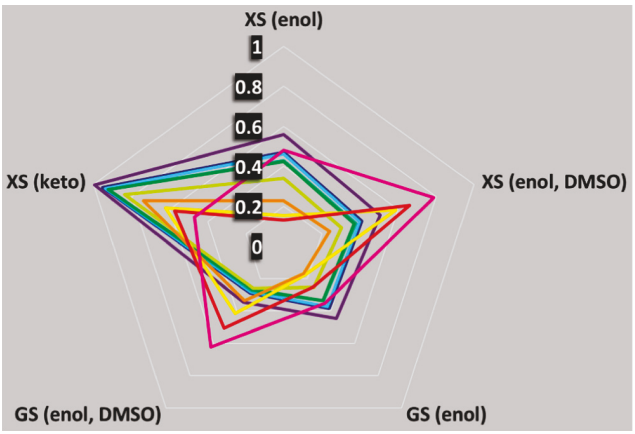


**Figure 19.** Energy gap (in eV) between LUMO + 1 and LUMO (ΔUMO) calculated at five optimized geometries of **PVHBO**s displayed on a radar plot. GS: ground state $S_0$; XS: excited state $S_1$. Only XS (keto) and XS (enol, DMSO) are emissive. The Hammett constant of the R substituent on the **PVHBO** increases based on the following order of colors: purple, blue, cyan, teal, green, lime, yellow, orange, red, and magenta. Each irregular pentagon connects the data of a given **PVHBO**.

gap between LUMO and LUMO + 1 (ΔUMO) at the optimized $S_0$ (GS; lower right in Figure 19) geometries diminishes, until the e-withdrawing power of R reaches Group II compounds where ΔUMO recovers. The break of the correlation between R and ΔUMO was observed in the $S_0$ of both intramolecular hydrogen-bonded and DMSO-hydrogen-bonded **PVHBO**s, as well as in the excited states of DMSO-hydrogen-bonded **PVHBO**s (Figure 19). The trend of ΔUMO vs Hammett constant remains largely unbroken in the excited intramolecularly hydrogen-bonded keto forms (XS (keto) in Figure 19), which is consistent with the observation that the keto emissions of all **PVHBO**s are similar.

The localization preferences of FMOs at the $S_0$ geometries explain the difference in the absorption spectra of Groups I and II compounds, in which a low-absorbance long wavelength shoulder of Group I compounds is readily visible, while in the spectra of Group II compounds, such a shoulder is obscured by the strong $S_2$ absorption band (the allowed HOMO → LUMO transition on stilbenoid) that is close in energy with $S_1$ (HOMO → LUMO + 1 that involves charge transfer).

The two emissive species of the neutral form of a **PVHBO** are shown in Figure 18b. Conspicuously missing is the intramolecularly hydrogen-bonded enol species. The enol form of a **PVHBO** with a N···H−O hydrogen bond, which is the linchpin of ESIPT, affords completely the excited keto species and therefore the keto emission, while the enol species with an O···H−O hydrogen bond is too energetic to be populated based on calculation. In solvents that preserve intramolecular HBs (e.g., DCM, ACN), all **PVHBO**s emit almost exclusively at the keto band after the ESIPT that involves the HOMO on the stilbenoid and the LUMO on the HBO component (e.g., see Figure S41). In a strong HB basic solvent (e.g., DMSO), the solvent-bonded population would emit at the enol wavelength. For DMSO-hydrogen-bonded Group I compounds, a long decay of a charge-transfer emission was observed. HOMO (stilbenoid) → LUMO (HBO) transition is principally responsible for the charge-transfer emission with a long lifetime (Figure 18b). For DMSO-hydrogen-bonded Group II compounds, first, the major contributing HOMO (stilbenoid) → LUMO (stilbenoid) is now localized on the stilbenoid and consequently has a large oscillator strength. Second, the HB between DMSO and the enol species is shortened relative to those in Group I compounds and exhibits a higher level of strengthening in the $S_1$ state than Group I compounds (Table 10). The strengthened hydrogen bonds in the excited state facilitate the excitation energy dissipation to the solvent and consequently the quenching of the enol emission by internal conversion.[79] Both factors would reduce the lifetime of the DMSO-hydrogen-bonded Group II enol species; however, the HB-mediated quenching would have to be the dominant factor. The keto emission that originates from the intramolecularly hydrogen-bonded species, on the other hand, is impacted relatively little by solvation. Therefore, it is preserved to become the dominant component in the steady-state emission. The evidence uncovered from this work suggests that the enol and keto emissions of any **PVHBO** originate from the solvent-hydrogen-bonded and intramolecularly hydrogen-bonded species, respectively, which are not in an equilibrium in the excited states.

With the assignment of emissive species (solvent-hydrogen-bonded enol and intramolecularly hydrogen-bonded keto) whose interconversion is interrupted by solvation (Scheme 2), and an understanding of R-dependent lifetime values (Figure 18b), an explanation on the trend of fluorescence quantum yields ($\phi$ values in Table 5) along either the change of R or solvent can be offered. In DMSO, Group I compounds have higher $\phi$ values than Group II compounds because the emissions of the solvent-hydrogen-bonded enol species of Group II compounds are quenched, while those of the solvent-bound Group I enol species are preserved. The lack of keto contribution to the emission of Group I compounds in polar solvents could be attributed to a secondary factor: the overall larger dipole moment of a Group I excited keto form than that of a Group II keto form (Table 9) may lead to a stronger solvation effect on Group I keto forms, which facilitates their internal conversion. In DCM, the $\phi$ values of Group II compounds are slightly but consistently larger than those of Group I compounds because the oscillator strengths of the excited keto species of Group II compounds are consistently larger (though not by much) than those of Group I compounds. In the absence of significant solvent-involved quenching (i.e., via intermolecular HBs), the oscillator strengths, which scale with the rates of radiative decays, could influence the magnitude of the $\phi$ values.

## CONCLUSIONS

In this paper, emission properties of **PVHBO**s that are structural fusions of stilbenoids and 2-(2′-hydroxyphenyl)-benzoxazole (HBO) are reported. The absorption and emission properties of these compounds that carry a substituent of various e-donating or e-withdrawing capabilities are characterized by solvents of different hydrogen-bonding abilities. The abrupt changes of absorption and solvent-dependent emission as the R group is becoming more e-withdrawing are explained by the facts uncovered from a computational study of the electronic properties of these compounds. **PVHBO**s act like hybrids of HBO and a stilbenoid by possessing ESIPT properties of the former and, as described in the succeeding paper, the emission property of


https://doi.org/10.1021/acs.jpca.1c10165
J. Phys. Chem. A 2022, 126, 1033−1061

the stilbenoid given the opportunity of intermolecular proton transfer (i.e., deprotonation). The nature of the R substituent on the stilbenoid determines the relative energies of LUMO and LUMO + 1 of a **PVHBO**, which, in conjunction with the physical residence of these two unoccupied molecular orbitals, have a defining effect on the absorption and solvent-dependent emission properties of these compounds. ESIPT only occurs in the species that contain intramolecular hydrogen bonds, while the enol emission observed in a hydrogen-bonding solvent is originated from the excited state that is hydrogen-bonded with the solvent. The dominance of the keto emission in a hydrogen-bonding solvent of the **PVHBO**s that carry e-withdrawing groups is explained by the quenching of the solvent-hydrogen-bonded excited enol species, rather than a more complete ESIPT that could be enabled by an e-withdrawing substituent. The interpretation based on the computational studies is consistent with the time-resolved emission and absorption data, which determine the ESIPT rates of **PVHBO**s in the range of 200−400 fs depending on the solvent and substituent and reveal the makeups of excited-state species within the limits of their time resolutions. The succeeding paper describes the emission properties of the deprotonated forms of **PVHBO**s and further demonstrates the effect of the R substituent on the multifaceted emission properties of these compounds that are affected by both intra- and intermolecular proton transfer in either ground or excited state.

## ■ ASSOCIATED CONTENT

### Supporting Information

The Supporting Information is available free of charge at https://pubs.acs.org/doi/10.1021/acs.jpca.1c10165.

Syntheses and characterizations; additional steady-state absorption and emission spectra; additional time-resolved absorption and emission spectra and kinetic decay traces; tables of lifetimes and amplitude values extracted from the time-resolved spectroscopic experiments; and additional computed figures (PDF)

## ■ AUTHOR INFORMATION


### Corresponding Author

**Lei Zhu** − *Department of Chemistry and Biochemistry, Florida State University, Tallahassee, Florida 32306-4390, United States;* orcid.org/0000-0001-8962-3666; Email: lzhu@fsu.edu

### Authors

**Quinton J. Meisner** − *Department of Chemistry and Biochemistry, Florida State University, Tallahassee, Florida 32306-4390, United States;* orcid.org/0000-0002-9342-0412

**Joseph J. M. Hurley** − *Department of Chemistry and Biochemistry, Florida State University, Tallahassee, Florida 32306-4390, United States*

**Peijun Guo** − *Center for Nanoscale Materials, Argonne National Laboratory, Lemont, Illinois 60439, United States;* Present Address: Department of Chemical and Environmental Engineering, Yale University, 520 West Campus Drive West Haven, CT 06516; orcid.org/0000-0001-5732-7061

**Anna R. Blood** − *New College of Florida, Sarasota, Florida 34243, United States*

**Richard D. Schaller** − *Center for Nanoscale Materials, Argonne National Laboratory, Lemont, Illinois 60439, United States;* orcid.org/0000-0001-9696-8830

**David J. Gosztola** − *Center for Nanoscale Materials, Argonne National Laboratory, Lemont, Illinois 60439, United States;* orcid.org/0000-0003-2674-1379

**Gary P. Wiederrecht** − *Center for Nanoscale Materials, Argonne National Laboratory, Lemont, Illinois 60439, United States*

Complete contact information is available at: https://pubs.acs.org/10.1021/acs.jpca.1c10165

### Author Contributions

‖Q.J.M. and J.J.M.H. contributed equally.


### Notes

The authors declare no competing financial interest.

## ■ ACKNOWLEDGMENTS

This work was supported by the National Science Foundation (CHE1566011 and CHE1955262 to L.Z.). The authors thank the NSF-Research Experiences for Undergraduates (REU) Sites program to support A.B. This material was based upon work supported by the NSF under Grant No. CHE-1659661. The late Professor Emeritus Ron Clark is acknowledged for performing X-ray single-crystal analysis. Use of the Center for Nanoscale Materials, an Office of Science user facility, was supported by the U.S. Department of Energy, Office of Science, Office of Basic Energy Sciences, under Contract No. DE-AC02-06CH11357.

## ■ REFERENCES


(1) Abou-Zied, O. K.; Jimenez, R.; Thompson, E. H. Z.; Millar, D. P.; Romesberg, F. E. Solvent-Dependent Photoinduced Tautomerization of 2-(2′-Hydroxyphenyl)benzoxazole. *J. Phys. Chem. A* **2002**, *106*, 3665−3672.

(2) Yuan, Z.; Tang, Q.; Sreenath, K.; Simmons, J. T.; Younes, A. H.; Jiang, D.-e.; Zhu, L. Absorption and Emission Sensitivity of 2-(2'-Hydroxyphenyl)benzoxazole to Solvents and Impurities. *Photochem. Photobiol.* **2015**, *91*, 586−598.

(3) Abou-Zied, O. K. Revealing the ionization ability of binding site I of human serum albumin using 2-(2′-hydroxyphenyl)benzoxazole as a pH sensitive probe. *Phys. Chem. Chem. Phys.* **2012**, *14*, 2832−2839.

(4) Heller, A.; Williams, D. L. Intramolecular proton transfer reactions in excited fluorescent compounds. *J. Phys. Chem. L* **1970**, *74*, 4473−4480.

(5) Mordziński, A.; Grabowska, A. Intramolecular Proton Transfer in Excited Benzoxazoles. *Chem. Phys. Lett.* **1982**, *90*, 122−127.

(6) Woolfe, G. J.; Melzig, M.; Schneider, S.; Dörr, F. The Role of Tautomeric and Rotameric Species in the Photophysics of 2-(2'-Hydroxyphenyl)benzoxazole. *Chem. Phys.* **1983**, *77*, 213−221.

(7) Krishnamurthy, M.; Dogra, S. K. Proton Transfer of 2-(2'-Hydroxyphenyl)benzoxazole in the Excited Singlet State. *J. Photochem.* **1986**, *32*, 235−242.

(8) Arthen-Engeland, T.; Bultmann, T.; Ernsting, N. P.; Rodriguez, M. A.; Thiel, W. Singlet Excited-State Intramolecular Proton Tranfer in 2-(2'Hydroxyphenyl)benzoxazole: Spectroscopy at Low Temperatures, Femtosecond Transient Absorption, and MNDO Calculations. *Chem. Phys.* **1992**, *163*, 43−53.

(9) Das, K.; Sarkar, N.; Ghosh, A. K.; Majumdar, D.; Nath, D. N.; Bhattacharyya, K. Excited-State Intramolecular Proton Transfer in 2-(2'-Hydroxyphenyl)benzimidazole and -benzoxazole: Effect of Rotamerism and Hydrogen Bonding. *J. Phys. Chem. Q* **1994**, *98*, 9126−0132.

(10) Rios, M. A.; Rios, M. C. Ab Initio Study of Ground and Excited State Proton Transfer in 2-(2'-Hydroxyphenyl)benzoxazole. *J. Phys. Chem. A* **1995**, *99*, 12456−12460.
(11) Wang, H.; Zhang, H.; Abou-Zied, O. K.; Yu, C.; Romesberg, F. E.; Glasbeek, M. Femtosecond fluorescence upconversion studies of excited-state proton-transfer dynamics in 2-(2'-hydroxyphenyl)-benzoxazole (HBO) in liquid solution and DNA. *Chem. Phys. Lett.* **2003**, *367*, 599−608.
(12) Kwon, J. E.; Park, S. Y. Advanced Organic Optoelectronic Materials: Harnessing Excited-State Intramolecular Proton Transfer (ESIPT) Process. *Adv. Mater.* **2011**, *23*, 3615−3642.
(13) Zhao, J.; Ji, S.; Chen, Y.; Guo, H.; Yang, P. Excited State Intramolecular Proton Transfer (ESIPT): from Principal Photophysics to the Development of New Chromophores and Applications in Fluorescent Molecular Probes and Luminescent Materials. *Phys. Chem. Chem. Phys.* **2012**, *14*, 8803−8817.
(14) Demchenko, A. P.; Tang, K.-C.; Chou, P.-T. Excited-State Proton Coupled Charge Transfer Modulated by Molecular Structure and Media Polarization. *Chem. Soc. Rev.* **2013**, *42*, 1379−1408.
(15) Sedgwick, A. C.; Wu, L.; Han, H.-H.; Bull, S. D.; He, X.-P.; James, T. D.; Sessler, J. L.; Tang, B. Z.; Tian, H.; Yoon, J. Excited-state intramolecular proton-transfer (ESIPT) based fluorescence sensors and imaging agents. *Chem. Soc. Rev.* **2018**, *47*, 8842−8880.
(16) D'Andrade, B. W.; Forrest, S. R. White Organic Light-Emitting Devices for Solid-State Lighting. *Adv. Mater.* **2004**, *16*, 1585−1595.
(17) Kamtekar, K. T.; Monkman, A. P.; Bryce, M. R. Recent Advances in White Organic Light-Emitting Materials and Devices (WOLEDs). *Adv. Mater.* **2010**, *22*, 572−582.
(18) Bao, L.; Heagy, M. D. A Review of Single White-Light Emitters: The Quest for Picture Perfect Dyes in the Next Generation of Single Layer WOLED Displays. *Curr. Org. Chem.* **2014**, *18*, 740−772.
(19) Meisner, Q. J.; Younes, A. H.; Yuan, Z.; Sreenath, K.; Hurley, J. J. M.; Zhu, L. Excitation-Dependent Multiple Fluorescence of a Substituted 2-(2′-Hydroxyphenyl)benzoxazole. *J. Phys. Chem. A* **2018**, *122*, 9209−9223.
(20) Hurley, J. J. M.; Meisner, Q. J.; Guo, P.; Schaller, R. D.; Wiederrecht, G. P.; Zhu, L. Triple Emission of 5'-(para-R-Phenylene)vinylene-2-(2'-Hydroxyphenyl)benzoxazole (PVHBO). Part II. Emission from the Anions. In press, DOI: 10.1021/acs.jpca.1c10167.
(21) Ahlrichs, R.; Bär, M.; Häser, M.; Horn, H.; Kölmel, C. Electronic Structure Calculations on Workstation Computers: The Program System Turbomole. *Chem. Phys. Lett.* **1989**, *162*, 165−169.
(22) Lee, C.; Yang, W.; Parr, R. G. Development of the Colle-Salvetti Correlation-Energy Formula into a Functional of the Electron Density. *Phys. Rev. B* **1988**, *37*, 785−789.
(23) Weigend, F.; Ahlrichs, R. Balanced Basis Sets of Split Valence, Triple Zeta Valence and Quadruple Zeta Valence Quality for H to Rn: Design and Assessment of Accuracy. *Phys. Chem. Chem. Phys.* **2005**, *7*, 3297−3305.
(24) Adamo, C.; Jacquemin, D. The Calculations of Excited-State Properties with Time-Dependent Density Functional Theory. *Chem. Soc. Rev.* **2013**, *42*, 845−856.
(25) Laaksonen, L. A Graphics Program for the Analysis and Display of Molecular Dynamics Trajectories. *J. Mol. Graphics* **1992**, *10*, 33−34.
(26) Bergman, D. L.; Laaksonen, L.; Laaksonen, A. Visualization of Solvation Structures in Liquid Mixtures. *J. Mol. Graphics Modell.* **1997**, *15*, 301−306.
(27) Christiansen, O.; Koch, H.; Jørgensen, P. The Second-Order Approximate Coupled Cluster Singles and Doubles Model CC2. *Chem. Phys. Lett.* **1995**, *243*, 409−418.
(28) Hättig, C.; Weigend, F. CC2 Excitation Energy Calculations on Large Molecules Using the Resolution of the Identity Approximation. *J. Chem. Phys.* **2000**, *113*, 5154−5161.
(29) Klamt, A.; Schüürmann, G. COSMO: a New Approach to Dielectric Screening in Solvents with Explicit Expressions for the Screening Energy and Its Gradient. *J. Chem. Soc. Perkin Trans. 2* **1993**, 799−805.
(30) Azarias, C.; Budzak, S.; Laurent, A. D.; Ulrich, G.; Jacquemin, D. Tuning ESIPT Fluorophores into Dual Emitters. *Chem. Sci.* **2016**, *7*, 3763−3774.
(31) Kim, C. H.; Park, J.; Seo, J.; Park, S. Y.; Joo, T. Excited State Intramolecular Proton Transfer and Charge Transfer Dynamics of a 2-(2′-Hydroxyphenyl)benzoxazole Derivative in Solution. *J. Phys. Chem. A* **2010**, *114*, 5618−5629.
(32) Chen, W.; Wright, B. D.; Pang, Y. Rational Design of a NIR-Emitting Pd(II) Sensor via Oxidative Cyclization to Form a Benzoxazole Ring. *Chem. Commun.* **2012**, *48*, 3824−3826.
(33) Benelhadj, K.; Muzuzu, W.; Massue, J.; Retailleau, P.; Charaf-Eddin, A.; Laurent, A. D.; Jacquemin, D.; Ulrich, G.; Ziessel, R. White Emitters by Tuning the Excited-State Intramolecular Proton-Transfer Fluorescence Emission in 2-(2'-Hydroxybenzofuran)benzoxazole Dyes. *Chem.−Eur. J.* **2014**, *20*, 12843−12857.
(34) Bergström, M.; Suresh, G.; Naidu, V. R.; Unelius, C. R.; N-Iodosuccinimide, N. I. S. in Direct Aromatic Iodination. *Eur. J. Org. Chem.* **2017**, *2017*, 3234−3239.
(35) Montalti, M.; Credi, A.; Prodi, L.; Gandolfi, M. T. *Handbooks of Photochemistry*, 3rd ed.; CRC Taylor and Francis, 2006; pp 624−628.
(36) Lin, T.-Y.; Tang, K.-C.; Yang, S.-H.; Shen, J.-Y.; Cheng, Y.-M.; Pan, H.-A.; Chi, Y.; Chou, P.-T. The Empirical Correlation between Hydrogen Bonding Strength and Excited-State Intramolecular Proton Transfer in 2-Pyridyl Pyrazoles. *J. Phys. Chem. A* **2012**, *116*, 4438−4444.
(37) Tseng, H.-W.; Liu, J.-Q.; Chen, Y.-A.; Chao, C.-M.; Liu, K.-M.; Chen, C.-L.; Lin, T.-C.; Hung, C.-H.; Chou, Y.-L.; Lin, T.-C.; et al. Harnessing Excited-State Intramolecular Proton-Transfer Reaction via a Series of Amino-Type Hydrogen-Bonding Molecules. *J. Phys. Chem. Lett.* **2015**, *6*, 1477−1486.
(38) Liu, Z.-Y.; Hu, J.-W.; Chen, C.-L.; Chen, Y.-A.; Chen, K.-Y.; Chou, P.-T. Correlation among Hydrogen Bond, Excited-State Intramolecular Proton-Transfer Kinetics and Thermodynamics for −OH Type Proton-Donor Molecules. *J. Phys. Chem. C* **2018**, *122*, 21833−21840.
(39) Xu, L.; Wang, Q.; Zhang, Y. Electronic effect on the photophysical properties of 2-(2-hydroxyphenyl)benzothiazole-based excited state intramolecular proton transfer fluorophores synthesized by Sonogashira-coupling reaction. *Dyes Pigm.* **2017**, *136*, 732−741.
(40) Smith, T. P.; Zaklika, K. A.; Thakur, K.; Barbara, P. F. Excited-State Intramolecular Proton Transfer in 1-(Acylamino)-anthraquinones. *J. Am. Chem. Soc.* **1991**, *113*, 4035−4036.
(41) Smith, T. P.; Zaklika, K. A.; Thakur, K.; Walker, G. C.; Tominaga, K.; Barbara, P. F. Spectroscopic studies of excited-state intramolecular proton transfer in 1-(acylamino)anthraquinones. *J. Phys. Chem. B* **1991**, *95*, 10465−10475.
(42) Jang, D. J.; Kelley, D. F. Time-resolved and steady-state fluorescence studies of the excited-state intramolecular proton transfer and relaxation of 2-hydroxy-4,5-naphthotropone. *J. Phys. Chem. C* **1985**, *89*, 209−211.
(43) Fukuda, M.; Terazima, M.; Kimura, Y. Study on the excited state intramolecular proton transfer of 4′-N,N-diethylamino-3-hydroxyflavone in imidazolium-based room temperature ionic liquids. *Chem. Phys. Lett.* **2008**, *463*, 364−368.
(44) Gauden, M.; Pezzella, A.; Panzella, L.; Neves-Petersen, M. T.; Skovsen, E.; Petersen, S. B.; Mullen, K. M.; Napolitano, A.; d'Ischia, M.; Sundström, V. Role of Solvent, pH, and Molecular Size in Excited-State Deactivation of Key Eumelanin Building Blocks: Implications for Melanin Pigment Photostability. *J. Am. Chem. Soc.* **2008**, *130*, 17038−17043.
(45) Ciuciu, A. I.; Skonieczny, K.; Koszelewski, D.; Gryko, D. T.; Flamigni, L. Dynamics of Intramolecular Excited State Proton Transfer in Emission Tunable, Highly Luminescent Imidazole Derivatives. *J. Phys. Chem. C* **2013**, *117*, 791−803.
(46) Ciuciu, A. I.; Flamigni, L.; Skonieczny, K.; Gryko, D. T. Blue-green emitting sulphonamido-imidazole derivatives: ESIPT based excited state dynamics. *Phys. Chem. Chem. Phys.* **2013**, *15*, 16907−16916.

(47) Kanosue, K.; Augulis, R.; Peckus, D.; Karpicz, R.; Tamulevičius, T.; Tamulevičius, S.; Gulbinas, V.; Ando, S. Polyimide and Imide Compound Exhibiting Bright Red Fluorescence with Very Large Stokes Shifts via Excited-State Intramolecular Proton Transfer II. Ultrafast Proton Transfer Dynamics in the Excited State. *Macromolecules* **2016**, *49*, 1848−1857.
(48) Skilitsi, A. I.; Agathangelou, D.; Shulov, I.; Conyard, J.; Haacke, S.; Mély, Y.; Klymchenko, A.; Léonard, J. Ultrafast photophysics of the environment-sensitive 4′-methoxy-3-hydroxyflavone fluorescent dye. *Phys. Chem. Chem. Phys.* **2018**, *20*, 7885−7895.
(49) Kumpulainen, T.; Lang, B.; Rosspeintner, A.; Vauthey, E. Ultrafast Elementary Photochemical Processes of Organic Molecules in Liquid Solution. *Chem. Rev.* **2017**, *117*, 10826−10939.
(50) McMorrow, D.; Kasha, M. Intramolecular Excited-State Proton Transfer in 3-Hydroxyflavone. Hydrogen-Bonding Solvent Pertubations. *J. Phys. Chem. D* **1984**, *88*, 2235−2243.
(51) Flom, S. R.; Barbara, P. F. Proton transfer and hydrogen bonding in the internal conversion of S1 anthraquinones. *J. Phys. Chem. E* **1985**, *89*, 4489−4494.
(52) Herbich, J.; Hung, C.-Y.; Thummel, R. P.; Waluk, J. Solvent-Controlled Excited State Behavior: 2-(2′-Pyridyl)indoles in Alcohols. *J. Am. Chem. Soc.* **1996**, *118*, 3508−3518.
(53) Waluk, J. Hydrogen-Bonding-Induced Phenomena in Bifunctional Heteroazaaromatics. *Acc. Chem. Res.* **2003**, *36*, 832−838.
(54) Takeuchi, S.; Tahara, T. Coherent Nuclear Wavepacket Motions in Ultrafast Excited-State Intramolecular Proton Transfer: Sub-30-fs Resolved Pump-Probe Absorption Spectroscopy of 10-Hydroxybenzo[h]quinoline in Solution. *J. Phys. Chem. A* **2005**, *109*, 10199−10207.
(55) Hohenberg, P.; Kohn, W. Inhomogeneous Electron Gas. *Phys. Rev.* **1964**, *136*, B864−B871.
(56) Kohn, W.; Sham, L. J. Self-Consistent Equations Including Exchange and Correlation Effects. *Phys. Rev.* **1965**, *140*, A1133−A1138.
(57) Gross, E. K. U.; Dobson, J. F.; Petersilka, M. *Density Functional Theory II: Relativistic and Time Dependent Extensions*; Nalewajski, R. F., Ed.; Springer Berlin Heidelberg: Berlin, Heidelberg, 1996; pp 81−172.
(58) Casida, M. E. *Recent Advances in Density Functional Methods*; Chong, D. P., Ed.; World Scientific: Singapore, 1995; Vol. *1*.
(59) Becke, A. D. Density-Functional Thermochemistry. III: The Role of Exact Exchange. *J. Chem. Phys.* **1993**, *98*, 5648−5652.
(60) Tirado-Rives, J.; Jorgensen, W. L. Performance of B3LYP Density Functional Methods for a Large Set of Organic Molecules. *J. Chem. Theory Comput.* **2008**, *4*, 297−306.
(61) Teramae, H.; Nagaoka, S.-i.; Nagashima, U. Computational Study of Excited-State Intramolecular-Proton-Transfer of *o*-Hydroxybenzaldehyde, O-Formyl-Substituted Phenols, and 5-Substituted Salicylaldehydes. *Int. J. Chem. Model.* **2012**, *4*, 269−287.
(62) de Vivie-Riedle, R.; De Waele, V.; Kurtz, L.; Riedle, E. Ultrafast Excited-State Proton Transfer of 2-(2′-Hydroxyphenyl)benzothiazole: Theoretical Analysis of the Skeletal Deformations and the Active Vibrational Modes. *J. Phys. Chem. A* **2003**, *107*, 10591−10599.
(63) Aquino, A. J. A.; Lischka, H.; Hättig, C. Excited-State Intramolecular Proton Transfer: A Survey of TDDFT and RI-CC2 Excited-State Potential Energy Surfaces. *J. Phys. Chem. A* **2005**, *109*, 3201−3208.
(64) Georgieva, I.; Trendafilova, N.; Aquino, A. J. A.; Lischka, H. Excited-State Proton Transfer in 7-Hydroxy-4-methylcoumarin along a Hydrogen-Bonded Water Wire. *J. Phys. Chem. A* **2007**, *111*, 127−135.
(65) Zhou, P.; Han, K. Unraveling the Detailed Mechanism of Excited-State Proton Transfer. *Acc. Chem. Res.* **2018**, *51*, 1681−1690.
(66) Nagaoka, S.-i.; Uno, H.; Huppert, D. Ultrafast Excited-State Intramolecular Proton Transfer of Aloesaponarin I. *J. Phys. Chem. B* **2013**, *117*, 4347−4353.
(67) Wilbraham, L.; Savarese, M.; Rega, N.; Adamo, C.; Ciofini, I. Describing Excited State Intramolecular Proton Transfer in Dual Emissive Systems: A Density Functional Theory Based Analysis. *J. Phys. Chem. B* **2015**, *119*, 2459−2466.
(68) Sobolewski, A. L.; Domcke, W. Computational Studies of the Photophysics of Hydrogen-Bonded Molecular Systems. *J. Phys. Chem. A* **2007**, *111*, 11725−11735.
(69) Houari, Y.; Charaf-Eddin, A.; Laurent, A. D.; Massue, J.; Ziessel, R.; Ulrich, G.; Jacquemin, D. Modeling Optical Signatures and Excited-State Reactivities of Substituted Hydroxyphenylbenzoxazole (HBO) ESIPT Dyes. *Phys. Chem. Chem. Phys.* **2014**, *16*, 1319−1321.
(70) Wu, C.-H.; Karas, L. J.; Ottosson, H.; Wu, J. I.-C. Excited-state proton transfer relieves antiaromaticity in molecules. *Proc. Nat. Acad. Sci. U.S.A.* **2019**, *116*, 20303−20308.
(71) Chrayteh, A.; Ewels, C. P.; Jacquemin, D. TD-DFT and CC2 insights into the dual-emissive behaviour of 2-(2′-hydroxyphenyl)-oxazoles core and their derivatives. *Phys. Chem. Chem. Phys.* **2020**, *22*, 25066−25074.
(72) Lampkin, B. J.; Nguyen, Y. H.; Karadakov, P. B.; VanVeller, B. Demonstration of Baird's rule complementarity in the singlet state with implications for excited-state intramolecular proton transfer. *Phys. Chem. Chem. Phys.* **2019**, *21*, 11608−11614.
(73) Louant, O.; Champagne, B.; Liégeois, V. Investigation of the Electronic Excited-State Equilibrium Geometries of Three Molecules Undergoing ESIPT: A RI-CC2 and TDDFT Study. *J. Phys. Chem. A* **2018**, *122*, 972−984.
(74) Wilson, J. N.; Josowicz, M.; Wang, Y.; Bunz, U. H. F. Cruciform p-Systems: Hybrid Phenylene-Ethynylene/Phenylene-Vinylene Oligomers. *Chem. Commun.* **2003**, 2962−2963.
(75) Clarke, T. M.; Gordon, K. C.; Kwok, W. M.; Phillips, D. L.; Officer, D. L. Tuning from $\pi,\pi^*$ to Charge-Transfer Excited States in Styryl-Substituted Terthiophenes: An Ultrafast and Steady-State Emission Study. *J. Phys. Chem. A* **2006**, *110*, 7696−7702.
(76) Bredas, J.-L. Mind the gap! *Mater. Horiz.* **2014**, *1*, 17−19.
(77) Sherin, P. S.; Grilj, J.; Tsentalovich, Y. P.; Vauthey, E. Ultrafast Excited-State Dynamics of Kynurenine, a UV Filter of the Human Eye. *J. Phys. Chem. B* **2009**, *113*, 4953−4962.
(78) Richert, S.; Mosquera Vazquez, S.; Grzybowski, M.; Gryko, D. T.; Kyrychenko, A.; Vauthey, E. Excited-State Dynamics of an Environment-Sensitive Push−Pull Diketopyrrolopyrrole: Major Differences between the Bulk Solution Phase and the Dodecane/Water Interface. *J. Phys. Chem. B* **2014**, *118*, 9952−9963.
(79) Dereka, B.; Vauthey, E. Direct local solvent probing by transient infrared spectroscopy reveals the mechanism of hydrogen-bond induced nonradiative deactivation. *Chem. Sci.* **2017**, *8*, 5057−5066.
(80) Chou, P.-T.; Yu, W.-S.; Cheng, Y.-M.; Pu, S.-C.; Yu, Y.-C.; Lin, Y.-C.; Huang; Chen, C.-T. Solvent-Polarity Tuning Excited-State Charge Coupled Proton-Transfer Reaction in p-N,N-Ditolylaminosalicylaldehydes. *J. Phys. Chem. A* **2004**, *108*, 6487−6498.
(81) Hsieh, C.-C.; Cheng, Y.-M.; Hsu, C.-J.; Chen, K.-Y.; Chou, P.-T. Spectroscopy and Femtosecond Dynamics of Excited-State Proton Transfer Induced Charge Transfer Reaction. *J. Phys. Chem. A* **2008**, *112*, 8323−8332.
(82) Chudoba, C.; Riedle, E.; Pfeiffer, M.; Elsaesser, T. Vibrational coherence in ultrafast excited state proton transfer. *Chem. Phys. Lett.* **1996**, *263*, 622−628.
(83) Lochbrunner, S.; Wurzer, A. J.; Riedle, E. Microscopic Mechanism of Ultrafast Excited-State Intramolecular Proton Transfer: A 30-fs Study of 2-(2′-Hydroxyphenyl)benzothiazole. *J. Phys. Chem. A* **2003**, *107*, 10580−10590.
(84) Lochbrunner, S.; Szeghalmi, A.; Stock, K.; Schmitt, M. Ultrafast proton transfer of 1-hydroxy-2-acetonaphthone: Reaction path from resonance Raman and transient absorption studies. *J. Chem. Phys.* **2005**, *122*, No. 244315.
(85) Schriever, C.; Barbatti, M.; Stock, K.; Aquino, A. J. A.; Tunega, D.; Lochbrunner, S.; Riedle, E.; de Vivie-Riedle, R.; Lischka, H. The interplay of skeletal deformations and ultrafast excited-state intramolecular proton transfer: Experimental and theoretical investigation of 10-hydroxybenzo[h]quinoline. *Chem. Phys.* **2008**, *347*, 446−461.


https://doi.org/10.1021/acs.jpca.1c10165
J. Phys. Chem. A 2022, 126, 1033−1061

(86) Schriever, C.; Lochbrunner, S.; Ofial, A. R.; Riedle, E. The origin of ultrafast proton transfer: Multidimensional wave packet motion vs. tunneling. *Chem. Phys. Lett.* **2011**, *503*, 61−65.
(87) Kim, C. H.; Joo, T. Coherent excited state intramolecular proton transfer probed by time-resolved fluorescence. *Phys. Chem. Chem. Phys.* **2009**, *11*, 10266−10269.
(88) Ameer-Beg, S.; Ormson, S. M.; Brown, R. G.; Matousek, P.; Towrie, M.; Nibbering, E. T. J.; Foggi, P.; Neuwahl, F. V. R. Ultrafast Measurements of Excited State Intramolecular Proton Transfer (ESIPT) in Room Temperature Solutions of 3-Hydroxyflavone and Derivatives. *J. Phys. Chem. A* **2001**, *105*, 3709−3718.
(89) Chou, P.-T.; Pu, S.-C.; Cheng, Y.-M.; Yu, W.-S.; Yu, Y.-C.; Hung, F.-T.; Hu, W.-P. Femtosecond Dynamics on Excited-State Proton/ Charge-Transfer Reaction in 4'-N,N-Diethylamino-3-hydroxyflavone. The Role of Dipolar Vectors in Constructing a Rational Mechanism. *J. Phys. Chem. A* **2005**, *109*, 3777−3787.
(90) Parada, G. A.; Markle, T. F.; Glover, S. D.; Hammarström, L.; Ott, S.; Zietz, B. Control over Excited State Intramolecular Proton Transfer and Photoinduced Tautomerization: Influence of the Hydrogen-Bond Geometry. *Chem.−Eur. J.* **2015**, *21*, 6362−6366.
(91) Kovalenko, S. A.; Ernsting, N. P.; Ruthmann, J. Femtosecond Stokes shift in styryl dyes: Solvation or intramolecular relaxation? *J. Chem. Phys.* **1997**, *106*, 3504−3511.
(92) Douhal, A.; Amat-Guerri, F.; Acuna, A. U. Photoinduced Intramolecular Proton Transfer and Charge Redistribution in Imidazopyridines. *J. Phys. Chem. B* **1995**, *99*, 76−80.
(93) Chou, P. T.; Martinez, M. L.; Cooper, W. C.; Collins, S. T.; McMorrow, D. P.; Kasha, M. Monohydrate catalysis of excited-state double-proton transfer in 7-azaindole. *J. Phys. Chem. F* **1992**, *96*, 5203−5205.
(94) Jang, D. J.; Brucker, G. A.; Kelley, D. F. Proton transfer in rare gas matrixes and ethanol solutions of 2-hydroxy-4,5-benzotropone. *J. Phys. Chem. G* **1986**, *90*, 6808−6811.
(95) Brucker, G. A.; Kelley, D. F. Spectroscopy and proton transfer of matrix-isolated hydrogen-bonding 3-hydroxychromone complexes. *J. Phys. Chem. H* **1987**, *91*, 2862−2866.
(96) Brucker, G. A.; Kelley, D. F. Proton transfer in matrix-isolated 3-hydroxyflavone and 3-hydroxyflavone complexes. *J. Phys. Chem. I* **1987**, *91*, 2856−2861.
(97) Inoue, H.; Hida, M.; Nakashima, N.; Yoshihara, K. Picosecond fluorescence lifetimes of anthraquinone derivatives. Radiationless deactivation via intra- and intermolecular hydrogen bonds. *J. Phys. Chem. J* **1982**, *86*, 3184−3188.
(98) Yatsuhashi, T.; Nakajima, Y.; Shimada, T.; Tachibana, H.; Inoue, H. Molecular Mechanism for the Radiationless Deactivation of the Intramolecular Charge-Transfer Excited Singlet State of Aminofluorenones through Hydrogen Bonds with Alcohols. *J. Phys. Chem. A* **1998**, *102*, 8657−8663.


https://doi.org/10.1021/acs.jpca.1c10165
*J. Phys. Chem. A* 2022, 126, 1033−1061